

Direct-Write Lithiation of Silicon Using a Focused Ion Beam of Li⁺

William R. McGehee,^{1‡} Evgheni Strelcov,^{1,2‡} Vladimir P. Oleshko,¹ Christopher Soles,¹ Nikolai B. Zhitenev,¹ and Jabez J. McClelland^{1}*

¹National Institute of Standards and Technology, Gaithersburg, MD 20899, USA

²Maryland NanoCenter, University of Maryland, College Park, MD 20742, USA

ABSTRACT Electrochemical processes that govern the performance of lithium ion batteries involve numerous parallel reactions and interfacial phenomena that complicate the microscopic understanding of these systems. To study the behavior of ion transport and reaction in these applications, we report the use of a focused ion beam of Li⁺ to locally insert controlled quantities of lithium with high spatial-resolution into electrochemically relevant materials *in vacuo*. To benchmark the technique, we present results on direct-write lithiation of 35 nm thick crystalline silicon membranes using a 2 keV beam of Li⁺ at doses up to 10¹⁸ cm⁻² (10⁴ nm⁻²). We confirm quantitative sub- μ m control of lithium insertion and characterize the concomitant morphological, structural and functional changes of the system using a combination of electron and scanning probe microscopy. We observe saturation of interstitial lithium in the silicon membrane at \approx 10 % dopant number density and spillover of excess lithium onto the membrane's surface. The implanted Li⁺ is demonstrated to remain electrochemically active. This technique will enable controlled studies and improve understanding of Li⁺ ion interaction with local defect structures and interfaces in electrode and solid-electrolyte materials.

KEYWORDS focused ion beams; ion implantation; nanoscale electrochemistry; Li-ion battery; transmission electron microscopy; KPFM

Progress in improving electrochemical devices is limited by our understanding of ionic transport and electrochemical transformation at the level of grain boundaries, interfaces, and single defects.¹ While the dynamics of these nanoscale processes control overall device performance, a quantitative understanding of the relevant processes in wet-cell experiments is often complicated by both the heterogeneous and parallel nature of these localized reactions. Accordingly, probes that provide more direct access to nanoscale ion dynamics are needed to explore the interplay between crystal structure, local defects, rate-limiting interfaces, the heterogeneous structure of materials, and the formation of solid-electrolyte interphases (SEI). Improved understanding of ionic transport and reactions will impact the work not only on traditional lithium ion batteries but also the broader space of electrochemically active systems including fuel cells² and resistive switching devices.^{3,4}

In recent years, several techniques for studying electrochemical systems at the nanoscale have been developed using scanning-probe microscopy (SPM) tip-based methods⁵⁻¹¹ and electron microscopy based techniques.¹²⁻¹⁷ These techniques have been used to explore nanoscale electrochemistry by driving reactions through nanostructures or through use of SPM conductive tips as electrodes. In the lithium-silicon system, this approach has enabled the observation of atomically-thin lithiation phase fronts and detailed studies of phase-front dynamics under strain.^{12,14,18-21} A limitation of these techniques is that they typically involve passive observation of the lithiation reaction, which is limited in part by the pre-existing local lithium concentration. For studies of heterogeneous materials, it is desirable to measure or modify the quantity of lithium that will react with specific structures in the absence of uncontrolled side reactions including SEI formation. Work on local quantitative delivery of Li⁺ has been undertaken using the SPM nanopipetting approach,⁷ but direct measurement of the locally deposited lithium proved challenging and estimates of Li concentration had to be made using SPM topographic maps.

Recently, Li⁺ focused ion beam (LiFIB) implantation has been proposed as a method to directly write known quantities of Li into battery materials to probe and modify lithium ionic systems. Similar ion beam technology is widely used in semiconductor processing for electronic doping, nanoscale milling, selective etching, and for chemical modification of material interfaces through ion beam mixing. Typical doses range from 10¹⁰ cm⁻² (10⁻⁴ nm⁻²) for light electronic doping of semiconductors to 10¹⁷ cm⁻² (10³ nm⁻²) for the etching process for silicon-on-insulator

manufacturing.²² Traditional application of ion beams to electrochemical systems center on the use of Ga⁺ FIBs for nanoscale milling or as part of transmission electron microscopy (TEM) sample preparation. Other battery-relevant work has used broad area implantation to increase adhesion between two dissimilar electrode layers²³ and to nanostructure the morphology of Ge electrodes in order to increase electrode capacity.²⁴ Broad area implantation using Li ions has been used to modify the electronic properties of Se nanowires²⁵ as well as to study amorphization and defects in Si.²⁶

Initial tests using LiFIB implantation of Sn micro-spheres demonstrated the qualitative utility of the technique for lithiating battery-relevant materials and compared ion implantation directly to electrochemical lithiation of similar structures.²⁷ In this work we demonstrate controlled, quantitative, low-energy implantation of Li⁺ ions into 35 nm thick crystalline silicon (*c*-Si) membranes using LiFIB. In particular, we demonstrate that the control afforded by a beam source of Li⁺ allows for local “titration” of the lithium concentration on a sub- μm length-scale. Implantation occurs *in vacuo* without formation of an SEI, electrolyte decomposition, or other parasitic reactions, enabling quantitative spatial control of lithium concentration such that individual structures in a material can be identified and then selectively implanted with sub-100 nm resolution. Unlike wet-cell lithiation, LiFIB implantation is not driven by local electrochemical potentials or phase-fronts in the material. Direct patterning of lithium concentration using the LiFIB will enable measurements of ionic transport with the ease of use afforded by focused beam implantation. Here, we establish LiFIB as a powerful tool for local lithiation of materials and discuss its advantages and limitations.

RESULTS AND DISCUSSION

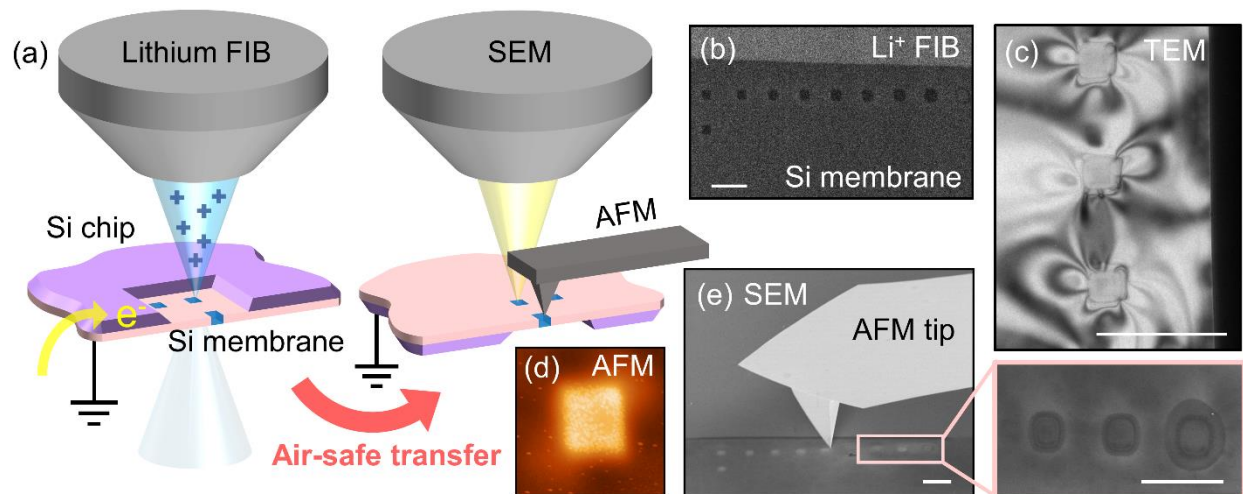


Figure 1. Schematic of Li^+ implantation into free standing, *c*-Si membranes and subsequent imaging. (a) A focused ion beam of Li^+ is used to pattern-implant controlled quantities of Li into 35 nm thick, *c*-Si membranes. The membrane is electrically grounded, and the implanted charge is compensated by electrons from ground. Further imaging of the implanted regions is performed on the opposite side of the membrane using electron and scanning probe microscopy after air-safe transfer to other instruments. (b) A Li^+ -induced secondary electron image taken after implantation shows ten, square $1\ \mu\text{m} \times 1\ \mu\text{m}$ regions implanted near the membrane's edge. (c) A bright-field TEM image shows three of these regions with extinction bend contours indicating the accumulation of local strain around the implanted regions. (d) AFM topography image shows expansion in the region of implantation; field-of-view is $3\ \mu\text{m}$. Color scale is from $-15\ \text{nm}$ (dark) to $50\ \text{nm}$ (bright). (e) SEM image shows an AFM tip scanning a dosed region on the membrane. Inset shows three dose regions with Li^+ fluence from $\approx 2500\ \text{nm}^{-2}$ to $\approx 5000\ \text{nm}^{-2}$. Scale bars are $5\ \mu\text{m}$.

Here, we study LiFIB implantation in crystalline silicon (*c*-Si), motivated by silicon's high specific capacity and promise as a next-generation Li anode material.²¹ The electrochemistry of silicon has been explored extensively and well-developed instrumentation is available for studying Si-based systems at the nanoscale, making Si an ideal material to benchmark the relevance of LiFIB implantation for electrochemical studies. Samples are prepared using the LiFIB to implant known quantities of Li^+ into free-standing, 35 nm thick membranes with ion fluence F_{Li} between $10\ \text{nm}^{-2}$ and $10^4\ \text{nm}^{-2}$. Morphological, structural, chemical, and functional changes to the membrane due to LiFIB implantation are characterized using a combination of scanning and stationary beam TEM analysis, scanning electron microscopy (SEM) imaging, and atomic force microscopy (AFM) as illustrated in Figure 1. Specifically, elemental composition mapping, including the implanted Li, is measured using electron energy loss spectroscopy (EELS) in the TEM. These compositional maps are used to validate the controlled, quantitative nature of the implantation. Morphological changes to the membrane are studied through a combination of AFM

topographic mapping paired with STEM-EELS spectral imaging, and Kelvin probe force microscopy (KPFM) is used to measure functional changes in the sample. The chemical nature of the beam-modified membrane is probed using spectral features in EELS, including the peak shifts of the bulk plasmon as well as the near-edge structure of the Li K transition. High-resolution TEM (HRTEM) is used to identify local structural changes in the implanted regions. The combination of these data provides a nuanced picture of the effects of Li⁺ ion implantation and are described in detail below.

The physical processes that occur during energetic ion implantation differ from those during electrochemical lithiation. The electrochemical lithiation of *c*-Si occurs through an atomically thin phase front of amorphous lithium silicide (*a*-Li_xSi), which expands into the native crystal, driven by a combination of electrical and chemical potentials using ions sourced from a liquid or solid electrolyte. The final state of lithiation is controlled by the applied potential, ending with amorphous Li₁₅Si₄ at room temperature.²¹ In contrast, the ion implantation discussed here physically embeds energetic Li⁺ ions into Si through an exposed surface in vacuum. The incident ions scatter in the silicon lattice through a rapid collisional cascade, creating damage as the ions scatter and slow.^{28,29} Bonding in the silicon lattice is disrupted during this process, but formation of equilibrium silicide compounds is not expected because of the rapid quenching of the incident ion energy as heat as well as damage created during the collisional cascade. The implanted Li⁺ ions are expected to be captured by ion-induced defects created within the Si lattice, thus forming metastable, partially crystalline phases with a high defect density. We label these ion-mixed phases as *i*-Li_xSi to distinguish them from the conventional *a*-Li_xSi formed during electrochemical lithiation. Conversion of *i*-Li_xSi into the equilibrium compounds can potentially be reached through thermal annealing (as in dopant activation used in traditional semiconductor processing).³⁰ The final state reached in ion implantation may also be affected by physical stresses that accumulate during implantation.^{18,31,32}

The collisional cascade of the ion beam occurs on a picosecond timescale, and these dynamics are well described by Monte Carlo simulations. The longitudinal range and lateral straggle in the material can be calculated by knowing the beam energy, ion mass, and the properties of incident material. Numerical simulation of 2 keV Li⁺ ions incident on a 35 nm Si membrane predict a mean longitudinal range of ≈ 18 nm with ≈ 85 % of the ions stopping in the membrane.³³

The remaining ions are predicted to either backscatter from ($\approx 9.2\%$) or transmit through ($\approx 5.4\%$) the membrane. Damage from the collisional cascade is primarily composed of Si interstitial-vacancy (Frenkel) pairs created at a rate of ≈ 40 per incident ion as well as accumulation of interstitial Li dopants. The Frenkel pairs in Si are known to anneal at room temperature with the damage accumulation controlled by competition between the dosing rate and thermal annealing of the silicon.²⁸ Sputtering of Si by light ions such as Li is calculated to be low (≈ 0.34 Si per incident ion), and self-sputtering of implanted Li may play a role at high doses. At room temperature, amorphization of Si due to relaxation of Frenkel pairs is expected for the dosing rates explored in this work.

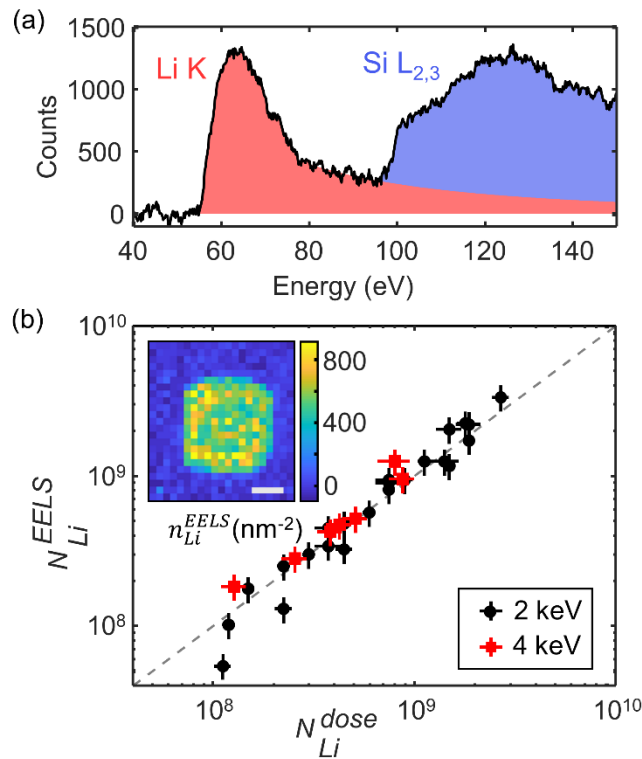


Figure 2. Quantification and mapping of Li using STEM-EELS. (a) Energy-loss spectrum for ion-implanted silicon (black line) containing the Li K (red shaded region) and the Si L_{2,3} (blue shaded region) transitions. Data are shown after deconvolution to remove plural scattering and with the low energy loss background subtracted. (b) Quantification of total Li dose in implanted regions is measured using EELS and compared to the implanted doses for beam energies of 2 keV (black circles) and 4 keV (red squares). The inset shows a representative map of Li areal density measured using EELS ($F_{Li} \approx 700 \text{ nm}^{-2}$) with 0.5 μm scale bar. Error bars (one standard deviation) indicate experimental uncertainty in the ion current and statistical uncertainty in measured dose.

As a first test of the utility of this technique, we compare the spatial profile of the implanted Li and the total Li dose from a series of implanted regions to those measured using EELS. A series of $1 \mu\text{m} \times 1 \mu\text{m}$ patterns are written into the membrane with ion fluence $F_{\text{Li}} = I_{\text{Li}}\tau/eA$ between 10^2 nm^{-2} and 10^4 nm^{-2} and beam energies of 2 keV and 4 keV (here I_{Li} is the beam current, τ is the dose time, e is the ion charge, and A is the implantation area). A characteristic EELS spectrum and map of the lithium areal density are shown in Figure 2. The measured total implanted Li dose $N_{\text{Li}}^{\text{EELS}}$ is calculated by summing the lithium areal density $n_{\text{Li}}^{\text{EELS}}$ map with known magnification over the lithium containing area. Areal densities are defined here as the atomic number density line-integrated through the thickness of the membrane. The *ab initio* number density for the pristine *c*-Si membrane $n_{\text{Si}} = \rho_{\text{Si}}h/m_{\text{Si}} \approx 1750 \text{ nm}^{-2}$, where ρ_{Si} is the silicon density, h is the membrane thickness, and m_{Si} is the Si atomic mass. The measured implanted dose is compared to the calculated implanted dose $N_{\text{Li}}^{\text{dose}} = I_{\text{Li}}\tau f/e$, where f is the fraction of the ion beam expected to stop in the membrane. Strong agreement is observed between $N_{\text{Li}}^{\text{dose}}$ and $N_{\text{Li}}^{\text{EELS}}$ over a factor of thirty in dose as shown in Figure 2b. Importantly, agreement is observed at both beam energies explored using stopping fractions $f_{2 \text{ keV}} \approx 0.85$ and $f_{4 \text{ keV}} \approx 0.54$, calculated using Monte Carlo scattering simulation.³³ These results show that ion implantation paired with numerical simulations enables precise, quantitative Li^+ patterning on a sub- μm length scale, even in partially ion-transparent materials.

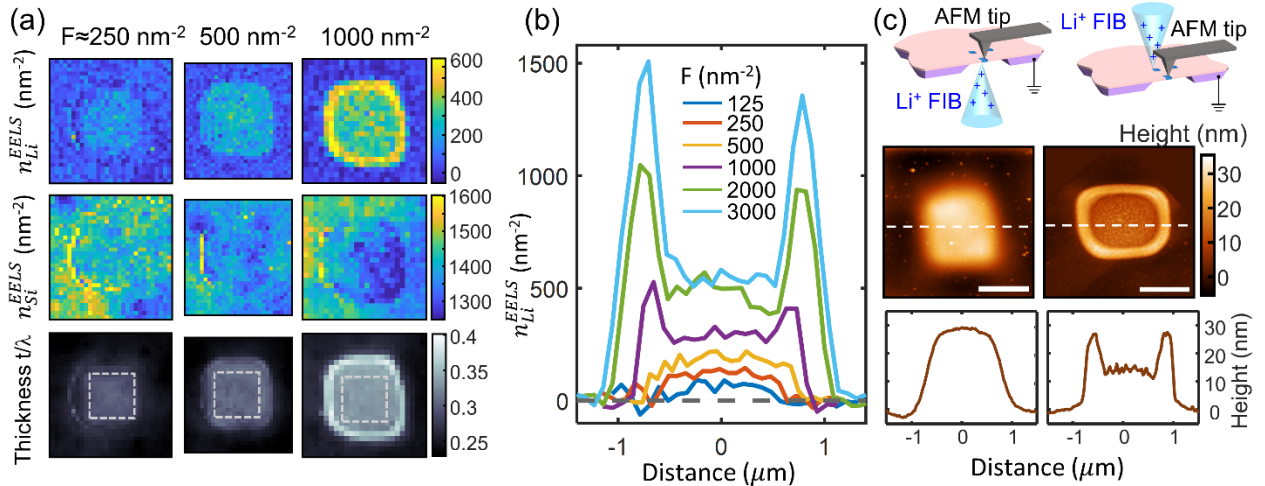


Figure 3. Morphological changes from ion implantation at 2 keV. (a) STEM-EELS mapping of Li and Si areal density as well as EELS thickness at $F_{\text{Li}} \approx 250 \text{ nm}^{-2}$, 500 nm^{-2} , and 1000 nm^{-2} (dashed boxes, $1 \mu\text{m} \times 1 \mu\text{m}$). Initial uniform increase in Li density is followed by Li accumulation around the edges of the implanted regions. (b) Slices of $n_{\text{Li}}^{\text{EELS}}$ through the center of the implanted regions

show saturation of the central lithium density and formation of spillover mounds on the periphery. (c) AFM topographic mapping shows distinct behaviors on the two sides of the membrane. The ion-implanted side (right column) shows large spillover areas, while the opposite side (left column) shows expansion only in the region of implantation. Scale bars are 0.5 μm . Traces show the difference in height measured across two different regions at $F_{\text{Li}} \approx 3300 \text{ nm}^{-2}$. Schematics indicate the relative orientation of ion implantation and AFM imaging (note: implantation and AFM measurements occurred in separate vacuum chambers).

The local injection of Li^+ ions into Si affects the morphology, structure, chemistry and functional properties of the material at the nanoscale. Below we describe these modifications sequentially with emphasis on the morphological changes due to implantation-induced amorphization and expansion of the membrane. An overview of the observed behavior is detailed in Figure 3a where EELS mapping shows that the measured Li areal density $n_{\text{Li}}^{\text{EELS}}$ and thickness t/λ (λ is the electron's inelastic mean free path in the sample) increase with ion dose while the measured silicon areal density $n_{\text{Si}}^{\text{EELS}}$ is largely unaffected by implantation. The observed distribution of Li matches the implantation pattern at low ion dose, but at higher doses Li is redistributed around the periphery of the implanted area. The progression from linear to non-linear implantation is shown in Figure 3b. The profiles show that the Li density within the implanted region saturates at high ion dose. The relatively minor differences between F_{Li} and $n_{\text{Li}}^{\text{EELS}}$ observed at $F_{\text{Li}} < 500 \text{ nm}^{-2}$ arise in part from the ion beam's pointing instability and the stopping fraction within the membrane. The disagreement at higher F_{Li} is dominated by ion-induced redistribution of Li (and not Si) onto the ion-incident surface of the membrane surrounding the implanted region. Expansion of the membrane is observed on both sides of the membrane as shown in Figure 3c, but formation of the peripheral "mounds" occurs only on the ion incident side.

An important observation in all measurements is the lack of diffusive ion transport after implantation. Both AFM and EELS signals measured within 1 hour of implantation closely match the deposition pattern used. Surprisingly, these signals do not change over a period of days, indicating that diffusion of Li out of the dosed regions is greatly restricted at room temperature. Given the amount of implanted lithium in our samples, we would have expected micron scale transport in several hours, because typical Li diffusion coefficients in amorphous and crystalline silicon are $\approx 10^{-12} \text{ cm}^2\text{s}^{-1}$ at 300 K for percent-level impurity concentrations.^{34,35} To explain the lack of diffusion in $i\text{-Li}_x\text{Si}$, we propose that the implanted Li atoms are bound to immobile, ion

beam induced point defects within the Si lattice, explaining the lack of diffusive Li transport observed in $i\text{-Li}_x\text{Si}$. Transport of Li in electrochemical lithiation of silicon can be also be slow due to the reaction-limited behavior at the phase front that forms between lithiated $a\text{-Si}$ and pristine $c\text{-Si}$.²¹ Similarly, strain at the boundary between $i\text{-Li}_x\text{Si}$ and pristine $c\text{-Si}$ may develop and contribute to stabilizing the implanted Li.

The saturation of $n_{\text{Li}}^{\text{EELS}}$ in the dosed region and mound formation appear to be driven by ion beam-induced mobility of the implanted Li. Implantation is experimentally realized by repeatedly rastering the ion beam over the desired area using a software-defined pattern. Implanted Li will be captured by the surplus of immobile point defects created in the lattice, but subsequent ion-irradiation can free these bound atoms for a short time, enabling motion within the membrane (until they are again captured by another defect or reach the membrane surface). This process is expected to occur throughout implantation, such that Li atoms are continuously freed and driven out of the beam path. Another consequence of ion irradiation is beam-induced disruption of the membrane surface, including the native oxide, which we speculate enables spillover of Li onto the membrane's surface. Surface Li may be rendered immobile, either through oxidation by background gas or captured by surface defects. These atoms are also driven out of the irradiated area by beam-induced mobility, leading to accumulation of Li in mounds on the membrane surface surrounding the irradiated area. These mounds extend hundreds of nanometers from the implanted region, likely impacted by the high surface mobility of Li^+ before fixation by the oxygen and water occur. Interestingly, we do not observe significant self-sputtering of Li. The beam-induced mobility discussed above limits the maximum n_{Li} achievable within the dosed region and hence the self-sputtering rate.

Spillover is observed primarily on the ion-incident surface of the membrane. At 2 keV beam energy, the ion's longitudinal range is biased toward the front (ion-incident) surface of the 35 nm thick membrane, leading to damage accumulation primarily on this surface rather than on the back surface of the membrane. Several samples implanted at the highest doses explored at 2 keV ($F_{\text{Li}} \approx 5 \times 10^3 \text{ nm}^{-2}$) and samples using 4 keV beam energy also showed spillover on the back surface of the membrane. At 4 keV, $\approx 45 \%$ of the Li^+ beam transmits through the membrane (compared to $\approx 5 \%$ at 2 keV), leading to significantly more damage on the far side of the membrane at constant F_{Li} . Our results indicate that there is likely a damage threshold past which

spillover occurs on the membrane surface. This threshold is reached easily on the ion-incident surface and on the far surface at the highest fluences explored. Due to this behavior, the scanning probe studies discussed below were performed on the back side of the membrane at 2 keV (where spillover is not observed). This configuration enables us to measure the properties of $i\text{-Li}_x\text{Si}$ and not those of the spillover material or beam-deposited carbon. Additionally, we operated below the fluence where spillover is observed on the back side of the membrane.

Structural changes after ion implantation, including amorphization and formation of nanocrystalline domains, were observed using HRTEM. A comparison of pristine and implanted regions within a Si membrane is shown in Figure 4a-c for $F_{\text{Li}} \approx 3300 \text{ nm}^{-2}$. This region shows a characteristic increase in thickness measured using EELS in both the implanted region as well as in the spillover area. HRTEM imaging in Figure 4b shows the initially pristine lattice in region A as well as the high degree of damage caused by ion implantation in region B . Disruption of the local crystal structure is evident, but the sample is not completely amorphized. Fourier analysis of the dosed region (B) shows that the original $c\text{-Si}$ diffraction peaks remain but are reduced to $\approx 20\%$ of their original amplitude. Additionally, two diffuse rings appear in the FFT image corresponding to interatomic spacing of $\approx 0.18 \text{ nm}$ and $\approx 0.32 \text{ nm}$. These diffraction patterns are consistent with a coexistence of $c\text{-Si}$ with amorphous $i\text{-Li}_x\text{Si}$ within the implanted region and the 0.32 nm ring is reminiscent of ordering observed in crystalline LiSi (see SI). Data acquired using selective-area electron diffraction (SAED) are consistent with these conclusions and show signatures of the presence of interstitials, likely Si or implanted Li (see SI).

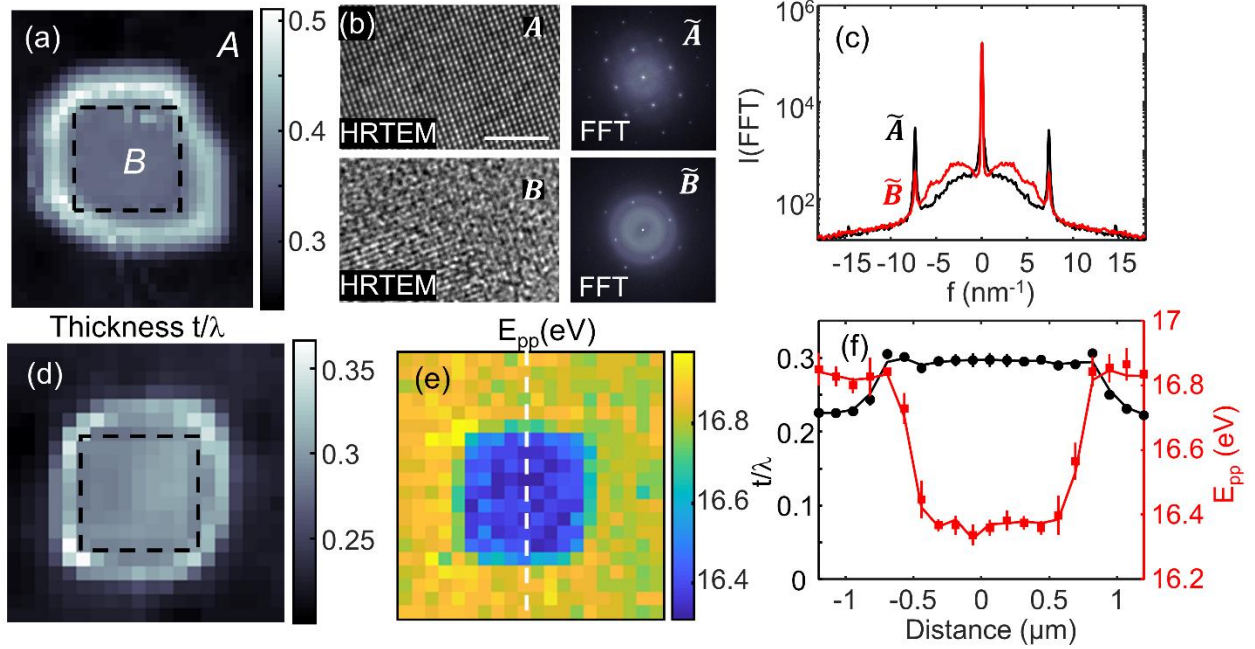


Figure 4. Structural changes in *c*-Si membrane from 2 keV ion implantation. (a) EELS thickness map of implanted region with $\approx 3.3 \times 10^9$ ($F_{\text{Li}} \approx 3300 \text{ nm}^{-2}$) implanted ions. The dashed box indicates the region of implantation ($1 \mu\text{m} \times 1 \mu\text{m}$). (b) HRTEM images acquired in regions *A* and *B* (scale bar is 2 nm), and FFT of areas *A* and *B* (magnitude shown on log scale), showing partial amorphization in the implanted region. (c) Averaged *k*-space profile of the pristine (black) and implanted (red) silicon shown along the [110] direction. (d) EELS thickness map for $1 \mu\text{m} \times 1 \mu\text{m}$ implanted region (dashed box) with $\approx 1.7 \times 10^9$ ($F_{\text{Li}} \approx 1700 \text{ nm}^{-2}$) implanted ions. (e) Map of the bulk plasmon peak energy E_{pp} measured using EELS. (f) Line profiles showing E_{pp} and EELS-measured membrane thickness along the dotted line in (e). Data are averaged over 5 adjacent pixels and errors bars represent the standard deviation of these values.

To determine the chemical state of the Li implanted Si, we analyze the plasmon excitations measured using EELS. The Si bulk plasmon is known to peak at $\approx 16.7 \text{ eV}$ for *c*-Si and at 16.3 eV for *a*-Si. The bulk plasmon for metallic Li peaks at $\approx 7.1 \text{ eV}$,³⁶ and oxidized forms of lithium (oxide, fluoride, carbonate, *etc.*) have peak plasmon energies between 19 eV and 25 eV , exceeding that of Si and many silicides.³⁷ The bulk plasmons for electrochemically cycled silicon and for thermodynamically stable Li-Si alloys have been observed to peak between 12 eV and 15 eV , varying based on their Li concentration.^{37,38} Mapping of the bulk plasmon for *i*-Li_xSi (center of dosed region in Figure 4d-f) shows that the peak plasmon energy E_{pp} is uniformly offset in the dosed region from the pristine value and is consistent with the spectrum of *a*-Si which peaks at 16.3 eV . We conclude that the dominant signal arises from *a*-Si, however other phases, including lithium silicide or lithium oxide, cannot be excluded due to the broad nature of the observed

features. Comparing the thickness map to the plasmon energy map in Figure 4c shows that amorphization occurs only within the 1 μm wide implantation region, and that Si below the spillover mounds remains crystalline, consistent with the expectation that the spillover mounds reside above the membrane surface. However, neither the metallic Li plasmon nor significant shifts of the plasmon peak due to the presence of the spillover mounds are observed. In a separate test, an attempt to measure the Li bulk plasmon in a thin metallic Li film (deposited from vapor onto a Si membrane with 3 nm to 10 nm thickness) showed that this low intensity peak may be masked by signals from the SiO_x/Si interface plasmon at ≈ 7.8 eV and the Si surface plasmon at ≈ 8.6 eV.³⁹ Further investigation is required to confirm or negate the presence of metallic Li in the spillover region.

Details about the chemical state of deposited Li can be gained through analysis of the energy loss near-edge structure (ELNES) of the Li K transition measured using EELS. The ELNES of the Li K-edge changes dramatically among common Li compounds,^{40,41} and the representative spectrum of the ion-beam lithiated silicon in Figure 2a shows a sharp rise near 55 eV with a single broad peak near 62 eV, consistent with published spectra of metallic Li. Most common Li compounds, such as lithium oxide or lithium carbonate, exhibit an eV-scale chemical shift in the K-edge threshold energy and contain additional identifying spectral features.⁴⁰ These signatures are not observed in air-safe transferred samples. One sample studied was inadvertently exposed to a fluorinated oil during transfer, and the Li K-edge ELNES was consistent with published LiF spectra, indicating the likely formation of LiF in that sample (see SI for more details). The majority of the samples were consistent with the presence of metallic Li captured by point defects within the lattice.

The morphological, structural and chemical transformations in the lithiated region cause functional changes in the electrical and electrochemical properties of the material. To probe these transformations, we use KPFM to measure contact potential difference (CPD) changes induced by implantation. CPD is defined as the difference between the electronic work functions of the AFM tip and sample (φ) normalized to the elementary charge e : $CPD = \frac{\varphi_{tip} - \varphi_{sample}}{e}$. The CPD is usually interpreted as an indicator of the Fermi level position for semiconductors/metallic samples, or electrostatic charge in insulating samples. However, from the electrochemical standpoint, CPD is

the Volta potential – a measure of the quasi-electrode potential of the system,[†] or its chemical oxidation state. Therefore, reduction of silicon by lithiation is expected to decrease its work function and increase its KPFM-measured CPD.

The observed changes in CPD and surface topography are measured for a range of 2 keV ion doses as shown in Figure 5. To measure the properties of *i*-Li_xSi (and not the properties of the spillover Li or beam-deposited carbon), imaging was performed on the membrane side opposite to the side of implantation (back side). For a given ion fluence, we observe the CPD in the implanted region CPD_{dosed} to be uniform within the noise of the measurement, and we measure the mean CPD shift relative to the neighboring pristine Si as $\Delta\text{CPD} = \text{CPD}_{\text{dosed}} - \text{CPD}_{\text{pristine}} = -(\varphi_{\text{Li}_x\text{Si}} - \varphi_{\text{Si}})/e$. Similarly, the magnitude of topographic changes is measured relative to the surrounding membrane as $\Delta H = |H_{\text{dosed}} - H_{\text{pristine}}|$. Both quantities are plotted in Figure 5g as a function of ion fluence. For these data, the area with modified CPD and topography largely match the shape of the target 1 μm^2 square implantation patterns. Note, that ΔH includes both the expansion of the membrane due to amorphization/lithiated phase formation and membrane buckling due to generated strain. For this reason, at low dose, the lithiated region is sometimes depressed relative to the rest of the membrane (inward buckling effect). Both ΔCPD and ΔH are observed to increase linearly with ion dose until a rough plateau is reached near a dose of $F_{\text{Li}} \approx 200 \text{ nm}^{-2}$ ($F_{\text{Li}} f_2 \text{ keV}/n_{\text{Si}} \approx 10 \%$, *i.e.* formal composition of Li_{0.1}Si). This plateau occurs before the dose at which spillover is observed on the ion-incident surface at $\approx 500 \text{ nm}^{-2}$ ($F_{\text{Li}} f_2 \text{ keV}/n_{\text{Si}} \approx 25 \%$).

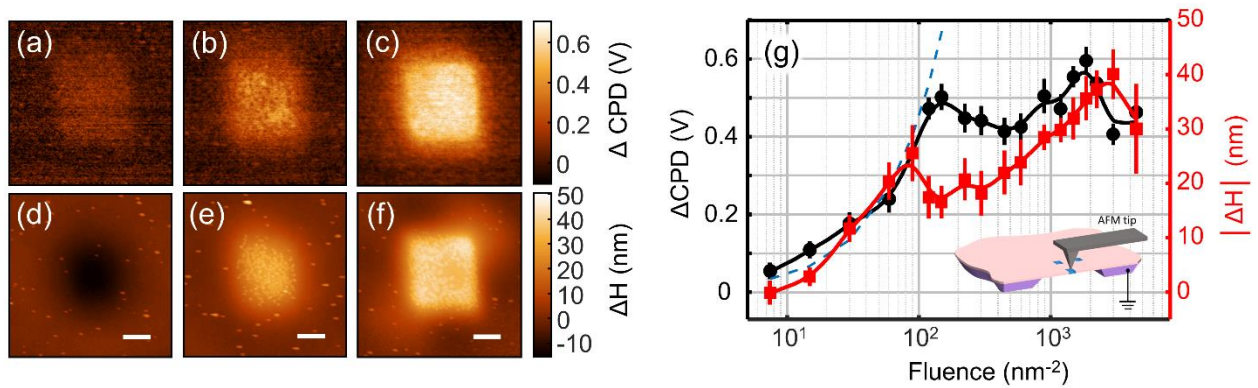


Figure 5. Functional changes of lithiated silicon measured using KPFM. (a-c) ΔCPD and (d-f) topography are measured on the front surface of the membrane (opposite to ion implantation) for

[†]Relative to the coating of the AFM tip

approximate ion doses of 30 nm^{-2} , 120 nm^{-2} , and 1500 nm^{-2} . Scale bar is $0.5 \mu\text{m}$ for all panels. (g) ΔCPD and the absolute value of height change averaged over the implanted region, plotted *versus* ion dose. Data represent the average value measured over the implanted region and error bars represent the standard deviation of the measurements across the same area. The dashed blue line indicates linear change with ion dose (drawn as a guide to the eye). Both ΔCPD and expansion form a plateau at $F_{\text{Li}} \approx 200 \text{ nm}^{-2}$. Inset indicates the orientation of AFM scanning.

The measured CPD maps indicate local, chemical reduction of the Si membrane due to ion implantation: $\text{Si} + x\text{Li}^+ + xe^- \rightarrow i\text{-Li}_x\text{Si}$ (electrons come from ground). A naïve interpretation of the increased CPD could be linked to positive implanted charge, however, the silicon will remain electrically neutral due to its high electronic conductivity. More generally, work functions (and, therefore, CPD) of pure elements are proportional to their Pauling electronegativity (Gordy-Thomas law), and chemical reduction commonly decreases the work function of a material. Examples of this phenomenon include reduction as a result of oxygen removal in transition metal oxides⁴² or as a result of intercalation of sodium or lithium into TiS_2 and V_2O_5 .^{40,41} In the latter case, formation of $\text{Li}_3\text{V}_2\text{O}_5$ from vanadium pentoxide decreased its work function by 2 eV (of which 1.4 eV was due to the surface dipole, and only 0.6 eV to the shift in the Fermi level).⁴² Hence, increased CPD (decreased work function) in the lithiated regions is not simply due to a shift in the Fermi level, but is consistent with reduction of the oxidation state of Si from 0 (in pristine Si) to $-x$ (in $i\text{-Li}_x\text{Si}$).

To gain a better understanding of the formation of $i\text{-Li}_x\text{Si}$ and the spillover regions, as well as distribution of lithium in depth, bulk Si wafers were LiFIB implanted and subsequently cross-sectioned using a conventional Ga^+ FIB as shown in Figure 6. Imaging of the exposed cross-section (not possible in 35 nm membranes) using SEM and KPFM provides additional information about the spatial distribution of implanted Li. KPFM provides a strong Li signal which is typically challenging to detect in bulk materials due to the low sensitivity of the Li K transition using X-ray techniques. Before cross-sectioning, the implanted region was capped with a protective layer of $\approx 1 \mu\text{m}$ thick, electron beam-deposited platinum to provide a sharp interface with the surface of the Si wafer and to enable smooth AFM scanning across the cross-sectioned interface (Fig. 6a). The implanted region is again $1 \mu\text{m} \times 1 \mu\text{m}$ with $F_{\text{Li}} \approx 1000 \text{ nm}^{-2}$; the cross-section was taken through the center of the implanted region so that both the spillover mounds and ion beam modified Si would be visible.

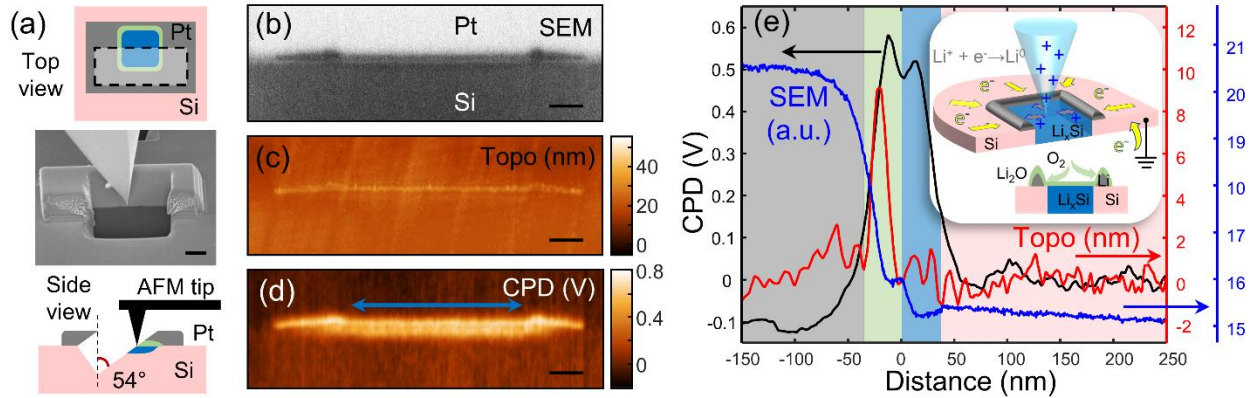


Figure 6. Cross section of ion-lithiated bulk silicon wafer. (a) Region is implanted at $F_{\text{Li}} \approx 1000 \text{ nm}^{-2}$ and milled with Ga^+ FIB at 54° relative to the surface normal. Schematic of the experiment shows lithiated Si (blue), spillover mounds (green), Pt layer (grey), and pristine Si (pink). The milled-away region is indicated by the dashed box. SEM image shows AFM scanning on the exposed surface (scale bar is $1 \mu\text{m}$). Images of the cross-sectioned surface are shown in: (b) SEM micrograph corrected for 54° -slope and contrast enhanced, (c) AFM topography with slope subtracted, and (d) KPFM CPD relative to pristine Si. Scale bars are 200 nm . Blue arrow indicates the width of the implanted region. (e) Profiles from the central region of (b-d) are plotted as a function of the calculated depth into the wafer with 0 indicating the Si-Pt interface as measured away from the implanted region. The background color regions indicate materials, as in (a). The inset shows a schematic of the formation of spillover regions during ion implantation in Si membranes. The implanted Li^+ is injected into silicon and is partly spilled over to the surface, moving to periphery, where it is reduced to metal by the incoming electron flow. Later the formed peripheral mounds slowly oxidize on the surface forming a $\text{Li}_2\text{O}/\text{LiOH}/\text{Li}_2\text{CO}_3$ crust.

Imaging of the exposed cross-section using SEM and KPFM shows two distinct bands of contrast that correspond to the spillover Li and the $i\text{-Li}_x\text{Si}$ as shown in Figure 6b-d. Profiles of these signals are overlaid in Figure 6e and show the variation in behavior as a function of the calculated depth into the wafer (dashed line in Fig. 6a). In particular, the peak in CPD inside the silicon (blue band) provides direct evidence for bulk material modification and not simply surface modification using LiFIB. The spillover band exists above the pristine surface of the Si wafer as seen in the SEM and CPD images, and its thickness is maximal around the outside of the deposited area, as expected from the preceding EELS and AFM measurements. Interestingly, a non-negligible amount of spillover exists above the implanted region, and this spillover resides entirely above the normal surface of the Si wafer. The spillover band is observed to protrude from the smooth-milled cross-section (Fig. 6c and 6e), implying its modification following milling. Since AFM imaging was performed immediately after milling and without breaking the vacuum

(normally 1×10^{-4} Pa, with a short spike to 1×10^{-2} Pa when the airlock is opened), the spillover material must be highly reactive to have been modified in this clean environment.

The contrast associated with the $i\text{-Li}_x\text{Si}$ is visible in both SEM and CPD images and shows that the lithiated region extends into the bulk of the Si wafer. The lateral width of the $i\text{-Li}_x\text{Si}$ band closely matches the $1 \mu\text{m}$ implantation pattern width (Fig 6d, blue arrow) and the measured CPD of ≈ 0.5 V relative to pristine Si is consistent with the KPFM measurements shown in Figure 5 for similar F_{Li} , supporting the assumption that the surface CPD measurements reflect the bulk properties of the membrane. The SEM and CPD profiles shown in Figure 6e show two overlapping peaks corresponding to the spillover material and lithiated silicon, with the $i\text{-Li}_x\text{Si}$ region peaking at ≈ 20 nm and extending to ≈ 50 nm below the pristine Si surface. This distance is comparable to the calculated ≈ 18 nm implantation depth for 2 keV implantation (note, that features in CPD maps appear wider due to KPFM artifacts, such as the tip cone contribution – see SI). Further evidence supporting LiFIB modification of bulk Si is detailed in the SI where SEM imaging of a cleaved interface after implantation shows similar contrast and confirms that the observed signal is not an artifact of Ga^+ FIB cross-sectioning. Further, the observation of spillover above the $i\text{-Li}_x\text{Si}$ region explains why the Li area density measured using EELS saturates at higher fluence than the saturation observed in CPD or expansion.

Taking all these observations into account, we propose the following mechanism of lithiation (refer to Fig. 6e inset schematic). Bombardment of the membrane with Li^+ ions constantly disrupts the Si-Si and the newly-forming Li-Si bonds, locally increasing the mobility of the Li^+ ions, which presumably repel each other (see SI). At a critical ion density, determined by the beam current, area, and membrane damage, Li^+ spills onto the front surface and migrates to the periphery. There, not being subject to further bombardment, ions capture an electron and form metallic lithium (as indicated by the low melting point of the mounded material – see SI). Compensation of the implanted positive charge likely happens by two spatially-separated reactions: in the implanted region, Si atoms are reduced and form amorphous lithium silicide (electrons come from ground): $x\text{Li}^+ + \text{Si} + xe^- \rightarrow i\text{-Li}_x\text{Si}$; on peripheral surface sites, where excess Li^+ ions spills over, mounds of metallic lithium is form: $\text{Li}^+ + e^- \rightarrow \text{Li}^0$. The surface Li is gradually oxidized by trace oxygen and water (residual pressure $\approx 10^{-4}$ Pa; Figure 6e, inset). Note that differentiating between metallic lithium and lithium oxide/hydroxide is difficult using KPFM, as

the work functions of these materials are very similar and sensitive to oxygen/water content (although the CPD of Li is higher than that of Li_2O).⁴³

The elemental composition of the mounds is confirmed by EELS mapping indicating the presence of Li, C, and O in these areas (see Figure S2, SI). The presence of C arises from trace hydrocarbons within the FIB chamber and peaks outside the implanted area. This result is consistent with imaging-induced deposition, and the C concentration is uncorrelated with the Li concentration indicating that it is unlikely to have reacted with the implanted Li. Spatial overlap of the O is seen with the Li map indicating that there is a layer of oxide crust on the spillover Li, which is formed *via* gradual oxidation of metallic lithium following deposition. Spillover and mound formation are not desirable in general, and suppression of these effects can be achieved by implantation into Si at reduced temperature, or implantation into other materials (*e.g.*, gold - see SI).

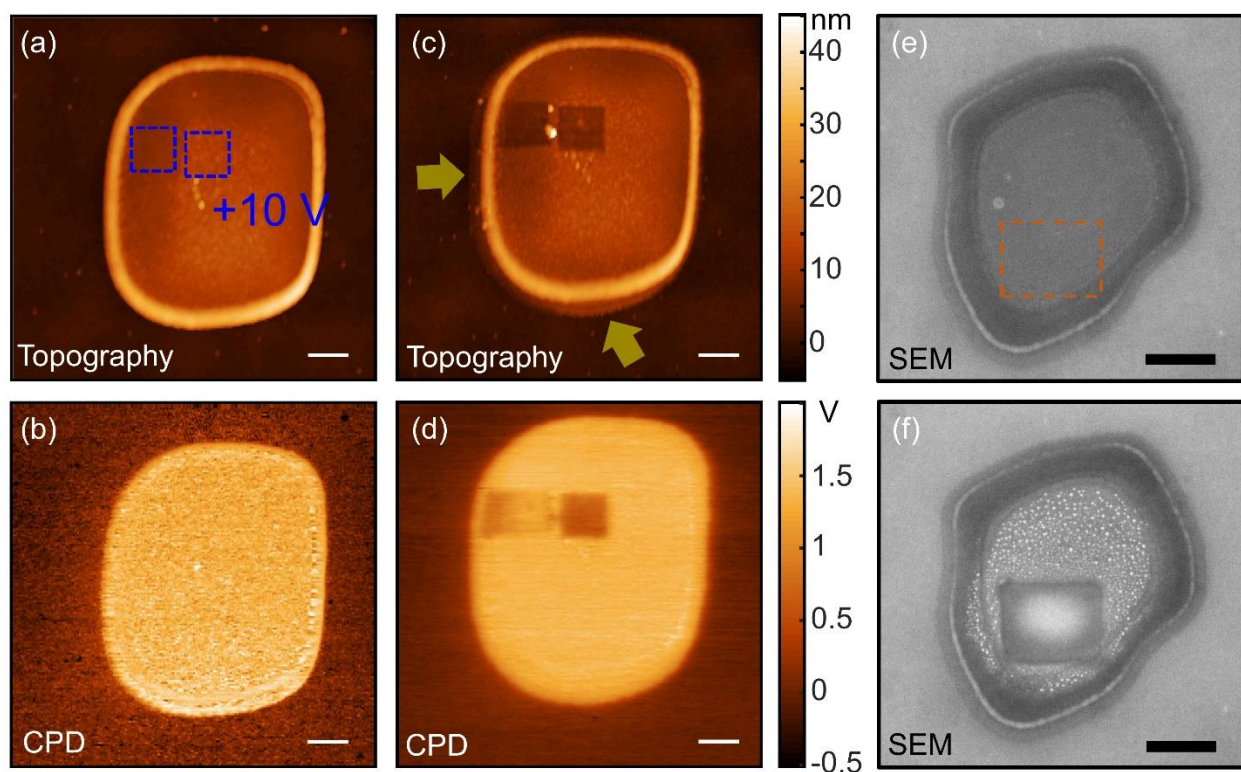
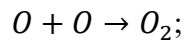
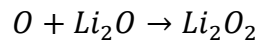
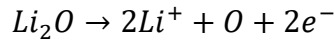


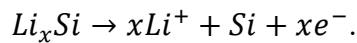
Figure 7. Reactivity of implanted lithium. (a)-(b) Topographic and KPFM images of a lithiated area on a 35 nm Si membrane ($2 \mu\text{m} \times 2 \mu\text{m}$, $F_{\text{Li}} \approx 1500 \text{ nm}^{-2}$). The two dashed $500 \text{ nm} \times 500 \text{ nm}$ blue boxes indicate regions that were scanned with a +10 V biased AFM tip in contact mode (while sample was grounded). (c)-(d) Topographic and CPD maps of the same area after biased scanning showing oxidation of the scanned regions and electromigration of lithium outward, beyond the peripheral mounds (indicated by yellow arrows). (e) SEM micrographs of another lithiated region

on the membrane ($1 \mu\text{m} \times 1 \mu\text{m}$, $F_{\text{Li}} \approx 630 \text{ nm}^{-2}$; the shape is distorted due to stage drift). The boxed area was irradiated by e-beam (2 kV, 140 pA) for several minutes. (f) SEM image of the same area following irradiation shows growth of nanocrystallites outside of the exposed area. The scale bars are 500 nm in all panels.

Although the implanted lithium remains stable at room temperature over days, it can be activated with temperature, an electron beam, or a biased AFM tip to illustrate that it is not idly bound and can be as reactive as lithium inserted into silicon by classical electrochemical methods. Figure 7a,b shows topographic and CPD KPFM images of a Si membrane area lithiated from the front. Clear peripheral mounds and a uniform high CPD region are seen. Two boxes were written by a +10 V biased conductive AFM tip in contact mode, as indicated by the blue. AFM imaging after biased scanning shows that the biased regions shrank and their CPD decreased to roughly half of the initial value relative to pristine Si (Figure 7c,d). Note, that charge injection from a +10 V biased tip cannot explain a decrease of the lithiated area CPD from its original value of about +1 V. The observed phenomenon is explained by electrochemical oxidation and delithiation of the materials under the biased AFM tip. We hypothesize that the following reactions may take place on the membrane surface:



and in the membrane bulk:



Here the lithium oxide crust on the surface and lithium silicide in the membrane's bulk decompose locally into compounds with higher work functions: solid Si, Li_2O_2 and adsorbed O_2 . The liberated Li^+ ions migrate away from the biased region and become reduced again to metallic lithium on the peripheral virtual cathode, expanding the mounds laterally, as indicated by the yellow arrows in Figure 7c. The CPD of the expanded areas and the initially formed mounds are similar, indicating that both are made of the same material – metallic lithium, oxidized from the surface. Biased AFM

scanning was also performed on regions with $F_{\text{Li}} \approx 100 \text{ nm}^{-2}$ where spillover effects were not observed and local delithiation of the ion mixed $i\text{-Li}_x\text{Si}$ phase was measured (see SI).

Reduction of the implanted Li into surface clusters was also observed with high-dose electron irradiation. Figure 7 shows a region before and after irradiation of 2 keV electrons at $F_{\text{Li}} \approx 630 \text{ nm}^{-2}$ within the orange box. Surface nanocrystals with diameter of $\approx 50 \text{ nm}$ are observed to slowly form. This observation is similar to reported Li plating in solid state batteries in which nucleation of Li microparticles or nanowires is found to be controlled by O concentration during battery cycling.⁴⁴ Formation of these nanocrystals occurs in the implanted region (not in the mounds), indicating that we are observing the reaction of Li from within the membrane. Thermal activation of implanted lithium is also possible, as shown in SI.

CONCLUSIONS

We have presented a method of direct-write, quantitative nanoscale lithiation of materials *in vacuo* using a focused lithium ion beam. Ion beam lithiation of 35 nm thick c-Si membranes occurs in two steps. At low ion dose ($F_{\text{Li}} \times f_{2 \text{ keV}}/n_{\text{Si}} \lesssim 0.1$), lithium areal density, surface expansion, and changes in the CPD all increase linearly with dose and their spatial distributions match their respective ion implantation patterns. The implanted regions are partially amorphized due to the accumulation of ion damage, and point defects in the Si lattice trap the implanted Li. This process leads to the formation of ion mixed, metastable $i\text{-Li}_x\text{Si}$. At high ion doses ($F_{\text{Li}} \times f_{2 \text{ keV}}/n_{\text{Si}} > 0.1$), the Li areal concentration and CPD saturate and Li spills over onto the ion-incident surface of the membrane. The spillover causes the formation of Li-rich mounds formed primarily around the periphery of the implanted areas which reside on the surface of the membrane. The spillover Li resides on the surface of the membrane and can be activated by direct biasing, electron irradiation, or thermal annealing.

The demonstrated local, quantitative lithiation of electrochemically relevant materials using the LiFIB will enable studies of ionic transport across nanostructures and exploration of the interplay of local strain, defect structure, grain boundaries, and other interfacial effects. These effects contribute to the overall performance of electrochemical systems, and understanding of the component processes in isolation benefits both the modelling and the development of future electrochemical devices. This technique is directly relevant for probing non-equilibrium and low-

concentration phases of lithiated materials that form because of incomplete lithium extraction and during the initial states of pristine anode lithiation. Future studies using this technique will explore thermal and electrically driven transport across grain boundaries to separate the role of bulk transport from that along the grain boundaries. Connection with traditional electrochemical experiments will be explored by driving ion implanted Li^+ from implanted structures with biased AFM tip to measure local rates of delithiation, activation energies, and Li^+ diffusivity.

METHODS

A low-energy, focused ion beams of Li^+ was created using a magneto-optical trap ion source (MOTIS).⁴⁵⁻⁴⁷ In this source, a neutral gas of ^7Li is laser-cooled to a temperature of $\approx 600 \mu\text{K}$, and a portion of this gas is photoionized in an electric field to form a beam with energy from 0.5 keV to 5 keV. The beam is rastered and focused using standard ion optics, and spots sizes of 30 nm to 100 nm are typically achieved with 1 pA to 30 pA current and 2 keV beam energy.⁴⁵ Software-defined patterns were used to raster the ion beam, and the ion current was measured using a Faraday cup attached to an ammeter. Spot sizes used were less than 100 m to enable uniform ion dosing using μm -scale patterns. Background gas pressure during implantation in the Li^+ FIB was $\approx 10^{-4} \text{ Pa}$ ($\approx 10^{-6} \text{ Torr}$). The sample was a free-standing, 35 nm thick (100)-oriented *c*-Si membrane (*p*-doped with dopant density of $\approx 10^{15} \text{ cm}^{-3}$ and conductivity of $\approx 10 \Omega \text{ cm}$). Reaction of the lithium implanted silicon with air was limited using air-safe transfer between the Li FIB and measurement chambers using a series of shuttles. Transfer between shuttles occurred in an Ar glove box (fractional oxygen and water content $\approx 10^{-7}$), and samples were transferred into the TEM using an Ar-flooded glove bag.

Atomic force microscopy (AFM) and Kelvin probe force microscopy (KPFM) were used to measure the modification of surface topography and contact potential difference (CPD) after ion implantation. KPFM was used in frequency-modulated mode with conductive Pt/Ir coated tips having resonance frequency between 65 kHz and 75 kHz and Q-factor of ≈ 3000 in vacuum. All AFM/KPFM imaging was performed *in vacuo* within the SEM chamber (residual pressure $\approx 10^{-4} \text{ Pa}$, $\approx 10^{-6} \text{ Torr}$), enabling simultaneous characterization of the sample using SEM and AFM, as well as precise placement of the AFM tip. AFM imaging was only possible on the non-recessed side of the membrane while SEM imaging was used on both sides. The sample was grounded during KPFM imaging. CPD maps were re-plotted by subtracting the average CPD value of Si

outside of the implanted region. For the data in Fig. 5, ions were implanted on the recessed side of the membrane to minimize the influence of carbon deposition on the KPFM measurements taken the opposite (flat) side of the sample. For comparison, ions were also implanted on the flat side of the membrane to record KPFM maps of the ion incident side of the membrane. For Figure 6, SEM image of the tilted surface was corrected by stretching the vertical axis by a factor of $1/\sin(54^\circ)$. KPFM images were re-scaled taken the SEM as a reference.

Transmission electron microscopy (TEM) was used to characterize microscopic structure including conventional TEM, high-resolution TEM (HRTEM) imaging, and selected-area electron diffraction (SAED) as well as for elemental mapping using electron energy loss spectroscopy (EELS). All images and spectra were acquired using 300 keV beam energy. The EELS thickness values t were calculated using the electron mean-free-path λ , the intensity I_0 of the zero-loss peak (ZLP), and the intensity of total spectrum I_Σ as $t/\lambda = \log[I_\Sigma/I_0]$.³⁶ Data shown here contain non-uniform composition, and the optical depth t/λ is quoted in all cases. The areal density n_k of element k with scattering channel cross-section σ_k is calculated using the intensity of the scattering I_k as $n_k = I_k/\sigma_k I_0$. Peaks corresponding to the Li K transition beginning at ≈ 55 eV and the Si L_{2,3} transition at ≈ 99 eV were used to quantify the line-integrated, areal density of these elements. Plural scattering effects were removed using Fourier-Log deconvolution.³⁶ The background in the remaining single-scattering spectrum was removed by fitting the pre-edge loss data to a power law distribution in energy, and I_k is the remaining signal integrated over a given energy window. The integrating windows and cross-sections used are detailed in the SI.

AUTHOR INFORMATION

Corresponding Author

jabez.mccllland@nist.gov, evgheni.strelcov@nist.gov

Author Contributions

All authors contributed to the conception of the experiment, interpretation of data, and writing of this manuscript. WRM led Li FIB implantation, ES led AFM characterization, and VO led TEM

characterization. All authors have given approval to the final version of this manuscript. ‡These authors contributed equally.

ASSOCIATED CONTENT

Supporting Information: The Supporting Information is available free of charge on the ACS Publications website at DOI.

EELS parameters, measurement showing limited O contamination, expanded explanation of cross-sectioned and cleaved implanted regions, measurements of thermal activation of implanted regions, measurement of spillover-free implantation, and electron diffraction images of implanted regions (PDF)

ACKNOWLEDGMENTS

The authors thank Andrei Kolmakov, Brian Hoskins, David Gundlach, Saya Takeuchi, John Cumings, Veronika Szalai, and Christopher Arble for helpful discussions. E.S. acknowledges support under the Cooperative Research Agreement between the University of Maryland and the National Institute of Standards and Technology Center for Nanoscale Science and Technology, Award 70NANB14H209, through the University of Maryland.

REFERENCES

- (1) Hausbrand, R.; Cherkashinin, G.; Ehrenberg, H.; Gröting, M.; Albe, K.; Hess, C.; Jaegermann, W. Fundamental Degradation Mechanisms of Layered Oxide Li-Ion Battery Cathode Materials: Methodology, Insights and Novel Approaches. *Mater. Sci. Eng. B* **2015**, *192*, 3–25.
- (2) Mahato, N.; Banerjee, A.; Gupta, A.; Omar, S.; Balani, K. Progress in Material Selection for Solid Oxide Fuel Cell Technology: A Review. *Prog. Mater. Sci.* **2015**, *72*, 141–337.
- (3) Strukov, D. B.; Snider, G. S.; Stewart, D. R.; Williams, R. S. The Missing Memristor Found. *Nature* **2008**, *453*, 80–83.
- (4) Waser, R.; Dittmann, R.; Staikov, G.; Szot, K. Redox-Based Resistive Switching Memories – Nanoionic Mechanisms, Prospects, and Challenges. *Adv. Mater.* **2009**, *21*, 2632–2663.

- (5) Balke, N.; Jesse, S.; Morozovska, A. N.; Eliseev, E.; Chung, D. W.; Kim, Y.; Adamczyk, L.; García, R. E.; Dudney, N.; Kalinin, S. V. Nanoscale Mapping of Ion Diffusion in a Lithium-Ion Battery Cathode. *Nat. Nanotechnol.* **2010**, *5*, 749–754.
- (6) Kalinin, S.; Balke, N.; Jesse, S.; Tselev, A.; Kumar, A.; Arruda, T. M.; Guo, S.; Proksch, R. Li-Ion Dynamics and Reactivity on the Nanoscale. *Mater. Today* **2011**, *14*, 548–558.
- (7) Larson, J. M.; Bharath, S. C.; Cullen, W. G.; Reutt-Robey, J. E. Scanning MWCNT-Nanopipette and Probe Microscopy: Li Patterning and Transport Studies. *Small* **2015**, *11*, 4946–4958.
- (8) Kruempelmann, J.; Balabajew, M.; Gellert, M.; Roling, B. Quantitative Nanoscopic Impedance Measurements on Silver-Ion Conducting Glasses Using Atomic Force Microscopy Combined with Impedance Spectroscopy. *Solid State Ion.* **2011**, *198*, 16–21.
- (9) Strelcov, E.; Mo Yang, S.; Jesse, S.; Balke, N.; K. Vasudevan, R.; V. Kalinin, S. Solid-State Electrochemistry on the Nanometer and Atomic Scales: The Scanning Probe Microscopy Approach. *Nanoscale* **2016**, *8*, 13838–13858.
- (10) Valov, I.; Sapezanskaia, I.; Nayak, A.; Tsuruoka, T.; Bredow, T.; Hasegawa, T.; Staikov, G.; Aono, M.; Waser, R. Atomically Controlled Electrochemical Nucleation at Superionic Solid Electrolyte Surfaces. *Nat. Mater.* **2012**, *11*, 530–535.
- (11) Wedig, A.; Luebben, M.; Cho, D.-Y.; Moors, M.; Skaja, K.; Rana, V.; Hasegawa, T.; Adepalli, K. K.; Yildiz, B.; Waser, R.; Valov, I. Nanoscale Cation Motion in TaO_x, HfO_x and TiO_x Memristive Systems. *Nat. Nanotechnol.* **2016**, *11*, 67–74.
- (12) McDowell, M. T.; Ryu, I.; Lee, S. W.; Wang, C.; Nix, W. D.; Cui, Y. Studying the Kinetics of Crystalline Silicon Nanoparticle Lithiation with *In Situ* Transmission Electron Microscopy. *Adv. Mater.* **2012**, *24*, 6034–6041.
- (13) Huang, J. Y.; Zhong, L.; Wang, C. M.; Sullivan, J. P.; Xu, W.; Zhang, L. Q.; Mao, S. X.; Hudak, N. S.; Liu, X. H.; Subramanian, A.; Fan, H.; Qi, L.; Kushima, A.; Li, J. *In Situ* Observation of the Electrochemical Lithiation of a Single SnO₂ Nanowire Electrode. *Science* **2010**, *330*, 1515–1520.
- (14) Liu, X. H.; Wang, J. W.; Huang, S.; Fan, F.; Huang, X.; Liu, Y.; Krylyuk, S.; Yoo, J.; Dayeh, S. A.; Davydov, A. V.; Mao, S. X.; Picraux, S. T.; Zhang, S.; Li, J.; Zhu, T.; Huang, J. Y. *In Situ* Atomic-Scale Imaging of Electrochemical Lithiation in Silicon. *Nat. Nanotechnol.* **2012**, *7*, 749–756.
- (15) Gu, M.; Parent, L. R.; Mehdi, B. L.; Unocic, R. R.; McDowell, M. T.; Sacci, R. L.; Xu, W.; Connell, J. G.; Xu, P.; Abellan, P.; Chen, X.; Zhang, Y.; Perea, D. E.; Evans, J. E.; Lauhon, L. J.; Zhang, J.; Liu, J.; Browning, N. D.; Cui, Y.; Arslan, I.; Wang, C. Demonstration of an Electrochemical Liquid Cell for Operando Transmission Electron Microscopy Observation of the Lithiation/Delithiation Behavior of Si Nanowire Battery Anodes. *Nano Lett.* **2013**, *13*, 6106–6112.
- (16) Yang, Y.; Gao, P.; Li, L.; Pan, X.; Tappertzhofen, S.; Choi, S.; Waser, R.; Valov, I.; Lu, W. D. Electrochemical Dynamics of Nanoscale Metallic Inclusions in Dielectrics. *Nat. Commun.* **2014**, *5*, 4232.
- (17) Strelcov, E.; Cothren, J.; Leonard, D.; Borisevich, A. Y.; Kolmakov, A. *In Situ* SEM Study of Lithium Intercalation in Individual V₂O₅ Nanowires. *Nanoscale* **2015**, *7*, 3022–3027.
- (18) Chon, M. J.; Sethuraman, V. A.; McCormick, A.; Srinivasan, V.; Guduru, P. R. Real-Time Measurement of Stress and Damage Evolution during Initial Lithiation of Crystalline Silicon. *Phys. Rev. Lett.* **2011**, *107*, 045503.

- (19) Balke, N.; Jesse, S.; Kim, Y.; Adameczyk, L.; Tselev, A.; Ivanov, I. N.; Dudney, N. J.; Kalinin, S. V. Real Space Mapping of Li-Ion Transport in Amorphous Si Anodes with Nanometer Resolution. *Nano Lett.* **2010**, *10*, 3420–3425.
- (20) Sternad, M.; Forster, M.; Wilkening, M. The Microstructure Matters: Breaking down the Barriers with Single Crystalline Silicon as Negative Electrode in Li-Ion Batteries. *Sci. Rep.* **2016**, *6*, 31712.
- (21) McDowell, M. T.; Lee, S. W.; Nix, W. D.; Cui, Y. 25th Anniversary Article: Understanding the Lithiation of Silicon and Other Alloying Anodes for Lithium-Ion Batteries. *Adv. Mater.* **2013**, *25*, 4966–4985.
- (22) Tong, Q.-Y.; Gösele, U. M. Wafer Bonding and Layer Splitting for Microsystems. *Adv. Mater.* **1999**, *11*, 1409–1425.
- (23) Rudawski, N. G.; Yates, B. R.; Holzworth, M. R.; Jones, K. S.; Elliman, R. G.; Volinsky, A. A. Ion Beam-Mixed Ge Electrodes for High Capacity Li Rechargeable Batteries. *J. Power Sources* **2013**, *223*, 336–340.
- (24) Rudawski, N. G.; Darby, B. L.; Yates, B. R.; Jones, K. S.; Elliman, R. G.; Volinsky, A. A. Nanostructured Ion Beam-Modified Ge Films for High Capacity Li Ion Battery Anodes. *Appl. Phys. Lett.* **2012**, *100*, 083111.
- (25) Panchal, S.; Chauhan, R. P. Lithium Ion Beam Impact on Selenium Nanowires. *Phys. E Low-Dimens. Syst. Nanostructures* **2017**, *87*, 37–43.
- (26) Oliviero, E.; David, M. L.; Fichtner, P. F. P.; Beaufort, M. F.; Barbot, J. F. Lithium Implantation at Low Temperature in Silicon for Sharp Buried Amorphous Layer Formation and Defect Engineering. *J. Appl. Phys.* **2013**, *113*, 083515.
- (27) Takeuchi, S.; McGehee, W. R.; Schaefer, J. L.; Wilson, T. M.; Twedt, K. A.; Chang, E. H.; Soles, C. L.; Oleshko, V. P.; McClelland, J. J. Editors' Choice Communication—Comparison of Nanoscale Focused Ion Beam and Electrochemical Lithiation in β -Sn Microspheres. *J. Electrochem. Soc.* **2016**, *163*, A1010–A1012.
- (28) Pelaz, L.; Marqués, L. A.; Barbolla, J. Ion-Beam-Induced Amorphization and Recrystallization in Silicon. *J. Appl. Phys.* **2004**, *96*, 5947–5976.
- (29) Caturla, M.-J.; Díaz de la Rubia, T.; Marqués, L. A.; Gilmer, G. H. Ion-Beam Processing of Silicon at keV Energies: A Molecular-Dynamics Study. *Phys. Rev. B* **1996**, *54*, 16683–16695.
- (30) Beyer, W.; Fischer, R.; Wagner, H. Lithium Doping of Amorphous Silicon. *J. Electron. Mater.* **1979**, *8*, 127–137.
- (31) Sethuraman, V. A.; Chon, M. J.; Shimshak, M.; Srinivasan, V.; Guduru, P. R. *In Situ* Measurements of Stress Evolution in Silicon Thin Films during Electrochemical Lithiation and Delithiation. *J. Power Sources* **2010**, *195*, 5062–5066.
- (32) Wan, W.; Zhang, Q.; Cui, Y.; Wang, E. First Principles Study of Lithium Insertion in Bulk Silicon. *J. Phys. Condens. Matter* **2010**, *22*, 415501.
- (33) Ziegler, J. F.; Ziegler, M. D.; Biersack, J. P. SRIM – The Stopping and Range of Ions in Matter (2010). *Nucl. Instrum. Methods Phys. Res. Sect. B Beam Interact. Mater. At.* **2010**, *268*, 1818–1823.
- (34) Ding, N.; Xu, J.; Yao, Y. X.; Wegner, G.; Fang, X.; Chen, C. H.; Lieberwirth, I. Determination of the Diffusion Coefficient of Lithium Ions in Nano-Si. *Solid State Ion.* **2009**, *180*, 222–225.
- (35) Tritsarlis, G. A.; Zhao, K.; Okeke, O. U.; Kaxiras, E. Diffusion of Lithium in Bulk Amorphous Silicon: A Theoretical Study. *J. Phys. Chem. C* **2012**, *116*, 22212–22216.

- (36) Egerton, R. F. *Electron Energy-Loss Spectroscopy in the Electron Microscope*, 3rd ed.; Springer US, **2011**; pp 231-291.
- (37) Boniface, M.; Quazuguel, L.; Danet, J.; Guyomard, D.; Moreau, P.; Bayle-Guillemaud, P. Nanoscale Chemical Evolution of Silicon Negative Electrodes Characterized by Low-Loss STEM-EELS. *Nano Lett.* **2016**, *16*, 7381–7388.
- (38) Danet, J.; Brousse, T.; Rasim, K.; Guyomard, D.; Moreau, P. Valence Electron Energy-Loss Spectroscopy of Silicon Negative Electrodes for Lithium Batteries. *Phys. Chem. Chem. Phys.* **2009**, *12*, 220–226.
- (39) Moreau, P.; Brun, N.; Walsh, C. A.; Colliex, C.; Howie, A. Relativistic Effects in Electron-Energy-Loss-Spectroscopy Observations of the Si/SiO₂ Interface Plasmon Peak. *Phys. Rev. B* **1997**, *56*, 6774–6781.
- (40) Wang, F.; Graetz, J.; Moreno, M. S.; Ma, C.; Wu, L.; Volkov, V.; Zhu, Y. Chemical Distribution and Bonding of Lithium in Intercalated Graphite: Identification with Optimized Electron Energy Loss Spectroscopy. *ACS Nano* **2011**, *5*, 1190–1197.
- (41) Muto, S.; Tatsumi, K. Detection of Local Chemical States of Lithium and Their Spatial Mapping by Scanning Transmission Electron Microscopy, Electron Energy-Loss Spectroscopy and Hyperspectral Image Analysis. *Microscopy* **2017**, *66*, 39–49.
- (42) Greiner, M. T.; Chai, L.; Helander, M. G.; Tang, W.-M.; Lu, Z.-H. Transition Metal Oxide Work Functions: The Influence of Cation Oxidation State and Oxygen Vacancies. *Adv. Funct. Mater.* **2012**, *22*, 4557–4568.
- (43) Yokota, T.; Suzuki, A.; Yamaguchi, K.; Terai, T.; Yamawaki, M. Study of the Tritium Behavior on the Surface of Li₂O by Means of Work Function Measurement. *J. Nucl. Mater.* **2000**, *283–287*, 1366–1369.
- (44) Yulaev, A.; Oleshko, V.; Haney, P.; Liu, J.; Qi, Y.; Talin, A. A.; Leite, M. S.; Kolmakov, A. From Microparticles to Nanowires and Back: Radical Transformations in Plated Li Metal Morphology Revealed via *In Situ* Scanning Electron Microscopy. *Nano Lett.* **2018**, *18*, 1644–1650.
- (45) Knuffman, B.; Steele, A. V.; Orloff, J.; McClelland, J. J. Nanoscale Focused Ion Beam from Laser-Cooled Lithium Atoms. *New J. Phys.* **2011**, *13*, 103035.
- (46) Twedt, K. A.; Chen, L.; McClelland, J. J. Scanning Ion Microscopy with Low Energy Lithium Ions. *Ultramicroscopy* **2014**, *142*, 24–31.
- (47) McClelland, J. J.; Steele, A. V.; Knuffman, B.; Twedt, K. A.; Schwarzkopf, A.; Wilson, T. M. Bright Focused Ion Beam Sources Based on Laser-Cooled Atoms. *Appl. Phys. Rev.* **2016**, *3*, 011302.

Supplemental Information for: Direct-Write Lithiation of Silicon Using a Focused Ion Beam of Li⁺

William R. McGehee,^{1,‡} Evgheni Strelcov,^{1, 2,‡} Vladimir P. Oleshko,¹ Christopher Soles,¹ Nikolai B. Zhitenev,¹ and Jabez J. McClelland^{1}*

¹National Institute of Standards and Technology, Gaithersburg, MD 20899, USA

²Maryland NanoCenter, University of Maryland, College Park, MD 20742, USA

I. EELS elemental mapping and quantification

EELS cross sections and energy windows used for elemental mapping are tabulated below. Electron beam energy used for all TEM/STEM imaging is 300 keV. Cross-sections are determined using the Hartree-Slater method.

Table S1: Parameters used for EELS analysis. Electron beam energy is 300 keV.

Transition	Cross-section (barns)	Energy window (eV)	Convergence Semi-angle (mrad)	Collection Semi-angle (mrad)
Li – K	46020	55 to 95	10	13
Si – L	42800	99 to 139	10	13
C – K	2863	283.9 to 323.9	10	32.5
O – K	805	531.9 to 571.9	10	32.5

II. Contamination during Li⁺ implantation and TEM imaging

The presence of O and C are also measured using EELS to determine the role of carbon deposition during imaging and reaction with O while under vacuum as well as during the transfer process. Images of n_{Li} , n_{C} , and n_{O} are plotted below for two high ion fluences. The presence of C arises from trace hydrocarbons within the FIB chamber and peaks outside the implanted area. This

result is consistent with ion-imaging-induced deposition, and the C concentration is uncorrelated with the Li concentration, indicating that it is unlikely to have reacted with the implanted Li. Spatial overlap of the O is seen with the Li map indicating that there must be a layer of oxide crust on the spillover Li, which is formed due to gradual oxidation of metallic lithium following deposition.

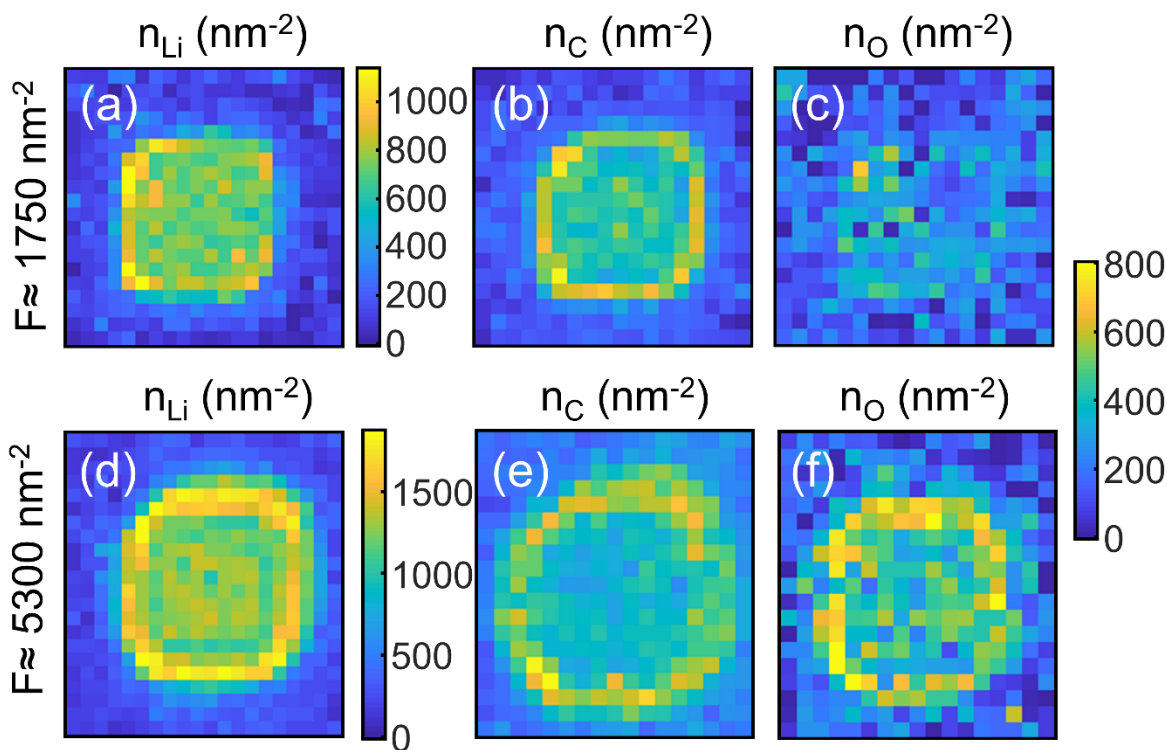


Figure S1 EELS mapping. a)-c) lithium, carbon and oxygen maps, respectively, measured on a Si membrane. The lithiated area was $1\ \mu\text{m} \times 1\ \mu\text{m}$, $F \approx 1750\ \text{nm}^{-2}$. d)-f) lithium, carbon and oxygen maps, respectively, measured on a Si membrane. The lithiated area was $1\ \mu\text{m} \times 1\ \mu\text{m}$, $F \approx 5300\ \text{nm}^{-2}$.

In addition to regular contamination/oxidation, in one instance, the sample was inadvertently exposed to a fluorine-containing material. This occasion helped us determine whether the ion-implanted Li is available to participate in further chemical reactions. The Li-implanted Si membrane was imaged using STEM/EELS on two separate days, and the EELS spectrum from a region was observed to change during the period between the two measurements. We suspect fluorinated vacuum grease (likely originating from an O-ring in the TEM sample holder) contaminated the sample and caused the Li-K line shape to change in a way consistent

with formation of LiF. The two spectra are shown in Figure S2. The initial spectrum (black) is consistent with the data shown in the main text as well as other samples that have been imaged. The spectrum acquired a day later (red) shows a clear modification of the shape of the Li-K line consistent with published values for LiF.¹ While the observed spectrum does not show the delayed edge threshold expected for LiF, this lack is likely a result of its being a combination of the initial Li-K peak shape and the spectrum associated with LiF.

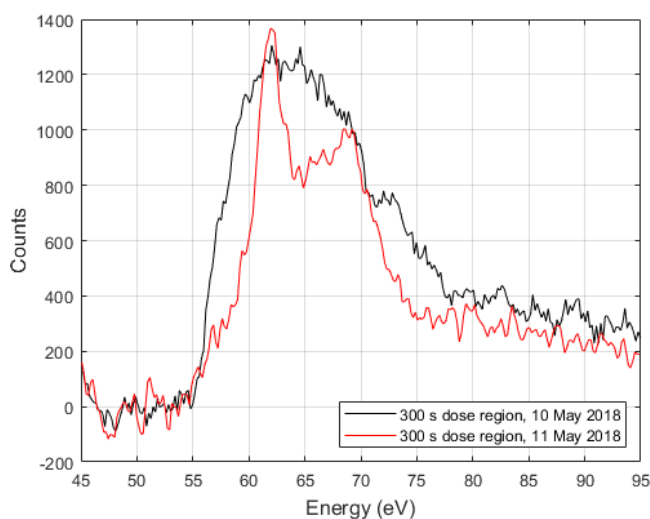


Figure S2. EELS spectrum containing Li K transition taken within several hours of implantation (black curve) and a spectrum taken the next day (red curve). Data are shown after deconvolution and with the background subtracted. Contamination with fluorine-based vacuum grease is likely responsible for the change in the spectrum.

III. Charge dynamics

We hypothesize that the dynamics of Li reduction are controlled in part by local electric fields along the surface of the membrane and by repulsion between charged ions in the membrane—to see this effect, a pair of circular implantation volumes were written close to each other as shown in Figure S3. In one pair the two circular regions were dosed sequentially (one circular region was dosed for 100 s followed by the second for 100 s). The next pair was written in parallel with the ion beam rapidly jumping back-and-forth between the two patterns every 20 ms until both had a total dose time of 50 s. In the patterns written sequentially, spillover mounds form uniformly around the circumference of each region—the same behavior that is observed for a single circular pattern in isolation. In contrast, the patterns written in parallel have spillover in two crescent-shaped regions on the distal ends of the pattern. Self-repelling Li^+ ions in the membrane move as far apart from each other as they can, leaving no mounds formed at the intersection of the

two circular patterns. The switching timescale for the parallel writing provides a lower bound for the reduction time scale in the membrane.

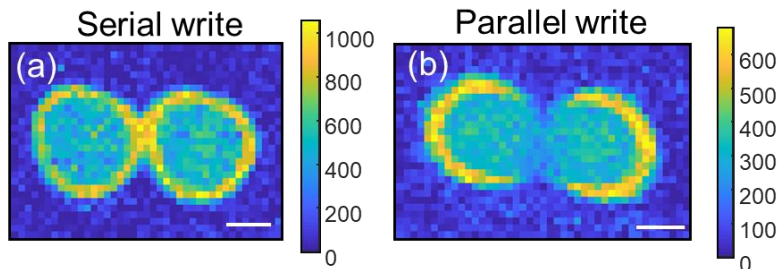


Figure S3. a) lithium map of a lithiated pattern on a Si membrane and consisting of two circular 1 μm diameter areas written in series. b) same, written in parallel. The scale bar is 500 nm.

IV. Cross-sectional view of implantation areas

As stated in the main text, Ga^+ FIB cross-sectioning helps to determine the structure of the lithiated area and surface spillover region. Figure S4a shows an SEM image of a cross-sectioned silicon-on-insulator (SOI) wafer which was lithiated, capped with Pt and milled. The SOI wafer is the same as was used for fabrication of the 35 nm-thick Si membranes. The spillover material and mounds are clearly seen under an e-beam-deposited platinum encapsulating layer, but the thin Si layer underneath is not well resolved. To gain insight into the processes under the Si surface, we lithiated a bulk Si wafer, as shown in Figure S4b-d (same as Fig. 6c-d, main text). Here, we provide more KPFM images in the zoomed-in boxes shown in Fig. S4d to provide a detailed view of the lithiated area and to ensure that the observed CPD distribution is not an artifact of KPFM scanning. Clearly, both trace and retrace (Fig. S4e-h) capture the double CPD band, corresponding to the surface spillover material and bulk lithiated silicon. The zoomed-in view of the “tails” of the cross-sectioned region (Fig. S4i-l) further demonstrate that the on-surface material extends laterally beyond the lithiated area (pink arrow). An SEM image of the AFM tip at the imaged interface is shown in Figure S4m. Note that the radius of the tip curvature is nominally about 25 nm, which is larger than the resolution of the presented KPFM images, implying that a nanoasperity at the tip’s apex must be responsible for the high resolution, as is common for in-vacuum FM-KPFM measurements.

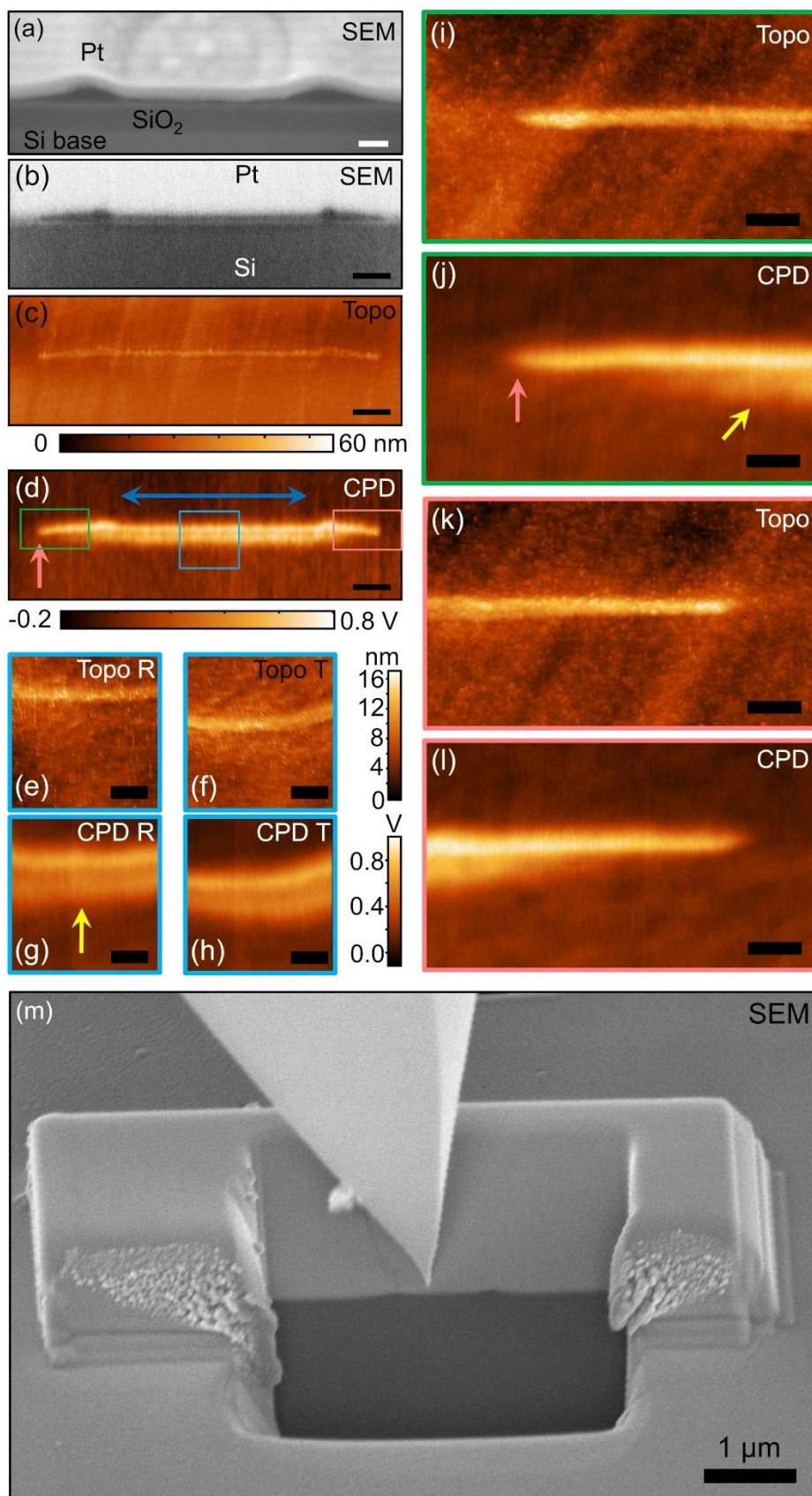


Figure S4. Cross-sectioning the lithiated areas. a) An SEM micrograph of a Ga^+ FIB-milled Li-implantation in an SOI wafer. The implanted area was capped with a Pt layer, seen on top. Below it are dark mounds and a 30 nm thick Si layer followed by the insulating SiO_2 layer and bulk Si base. The fluence for the implantation was $F \approx 1100 \text{ nm}^{-2}$ in $1 \mu\text{m} \times 1 \mu\text{m}$ area. The scale bar is 200 nm. b) An SEM micrograph of a similar cross-section performed on a bulk Si wafer lithiated with $F \approx 1000 \text{ nm}^{-2}$ in a $1 \mu\text{m} \times 1 \mu\text{m}$ area. Besides the dark mounds residing on the surface of Si, a dark band below the Si surface is seen, which corresponds to lithiated silicon. c) and d) Topographic and KPFM maps of the same region as in b). Additional scanning was performed inside the boxed areas and shown in panels (g), (h), (j) and (l) (CPD maps; color scale for all shown in (h)), and (e), (f), (i) and (k) (topographic maps; color scale for (i) and (k) is shown in (f)). For (e)-(h) both trace and retrace images are shown. The wide band of high CPD under the Si surface in the CPD maps (yellow arrows) is clear evidence for lithiation of Si below the spillover mound. Si is lithiated only under the $1 \mu\text{m} \times 1 \mu\text{m}$ implantation area, where the Li^+ FIB was rastered (indicated with blue arrow). The lithiation mound on the surface extends laterally beyond this region, as indicated by the pink arrow. KPFM imaging was performed right after milling, without breaking the vacuum. Scale bars in (a)-(c) are 200 nm; in (e)-(l) – 25 nm. (m) An SEM micrograph of the AFM tip parked in the milled area on the Pt-Si interface. The two mounds appear as dark protrusions into the Pt.

Although the under-the-Si-surface contrast is detected by two techniques with dissimilar contrast formation mechanisms (SEM and KPFM), it is possible that the bands observed in the images appear due to Pt deposition or Ga^+ ion implantation while the sample is cross-sectioned. To test this hypothesis, a bulk Si wafer was FIB-lithiated along a long narrow stripe and then cleaved perpendicular to the implanted stripe in an Ar atmosphere. The exposed, cleaved surface was imaged in SEM (Fig. S5). Despite the absence of Pt and Ga^+ implantation in this sample, a dark narrow band appears in bulk Si right under the lithiated strip. We conclude from this observation that the KPFM and SEM data shown previously are not significantly compromised by the sample cross-sectioning procedure.

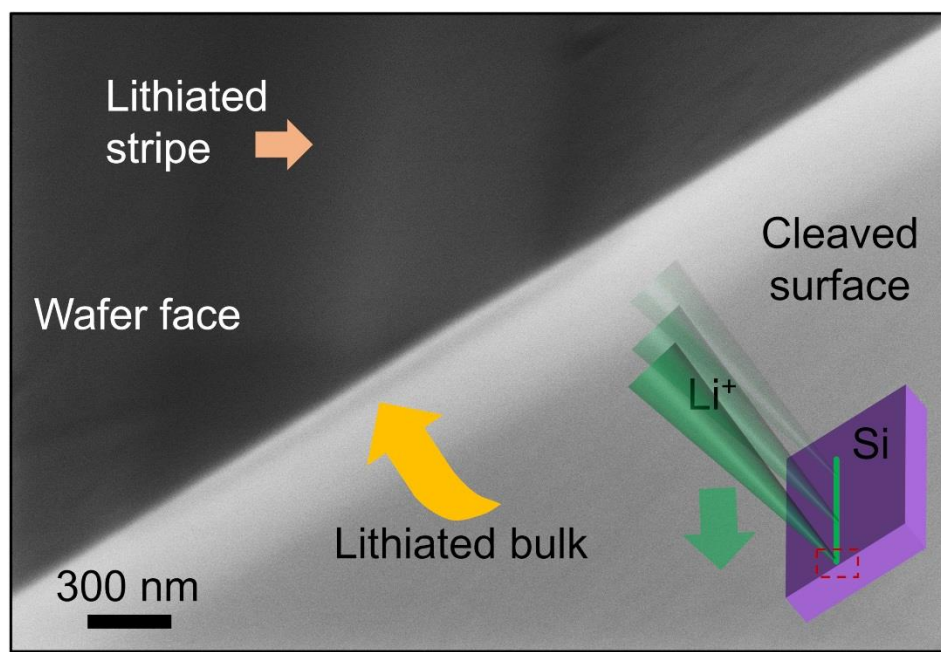


Figure S5. Cleaving a lithiated area. An SEM micrograph of a silicon wafer with a long lithiated stripe written on its face surface as indicated in the inset cartoon and by the orange arrow. Following lithiation, the wafer was cleaved perpendicular to the written line exposing the lithiated bulk (dark band indicated with yellow arrow).

V. Electrochemical activation (delithiation) without spillover

While the main text Figure 7 shows that activation of the injected Li^+ is possible at high lithium doses, when a spill-over region is formed, the question arises, whether same is true for the low-doses, when all the injected Li^+ remains in the Si. It is also important to verify that the material can be de-lithiated. To answer these questions, we have repeated the biased AFM tip experiment (see Fig. 7, main text and surrounding text) at low ion fluence ($F_{\text{Li}} \approx 100 \text{ nm}^{-2}$). At this ion fluence, spillover is not observed, and all implanted Li are expected to remain within the Si. Implantation was performed in a bulk Si wafer followed by AFM imaging, biased AFM scanning, and subsequent AFM imaging as shown in Figure S6. The implanted region (Fig. S6 a,b) has uniform expansion and CPD due to the implantation dose, characteristic of the linear response regime to implantation (no spill-over, or mounds). A halo is evident in the CPD signal surrounding the implanted region, likely due to ion beam instability (and reproduced in perpendicular AFM scanning of the same region). Two small, rectangular regions within the implanted area were scanned with the AFM tip in contact mode and with bias applied to the tip of +10 V and 0 V (Fig. S6a). Following biased scanning, a decrease in CPD of the lithiated area and accumulation of

surface particles are observed as shown in Fig. S6c, d. The rectangular region scanned with 0 V bias shows no change in topography or CPD relative to the regions that were not scanned in contact mode. The rectangular region scanned at +10 V shows a marked decrease in CPD—this is consistent with oxidation of this region and delithiation of the ion mixed $i\text{-Li}_x\text{Si}$ phase. We propose that local delithiation occurred according to: $\text{Li}_x\text{Si} \rightarrow x\text{Li}^+ + \text{Si} + xe^-$. Since no excess Li^+ is observed in the periphery of the implanted region (unlike the example shown in Figure 7, main text), it is assumed that the liberated Li^+ ions migrated deeper into the bulk of the wafer and are not detected by KPFM. These data show that Li^+ in the ion mixed $i\text{-Li}_x\text{Si}$ phase (in the absence of spill-over material) remains electrochemically-active and can be driven spatially by application of suitable potentials.

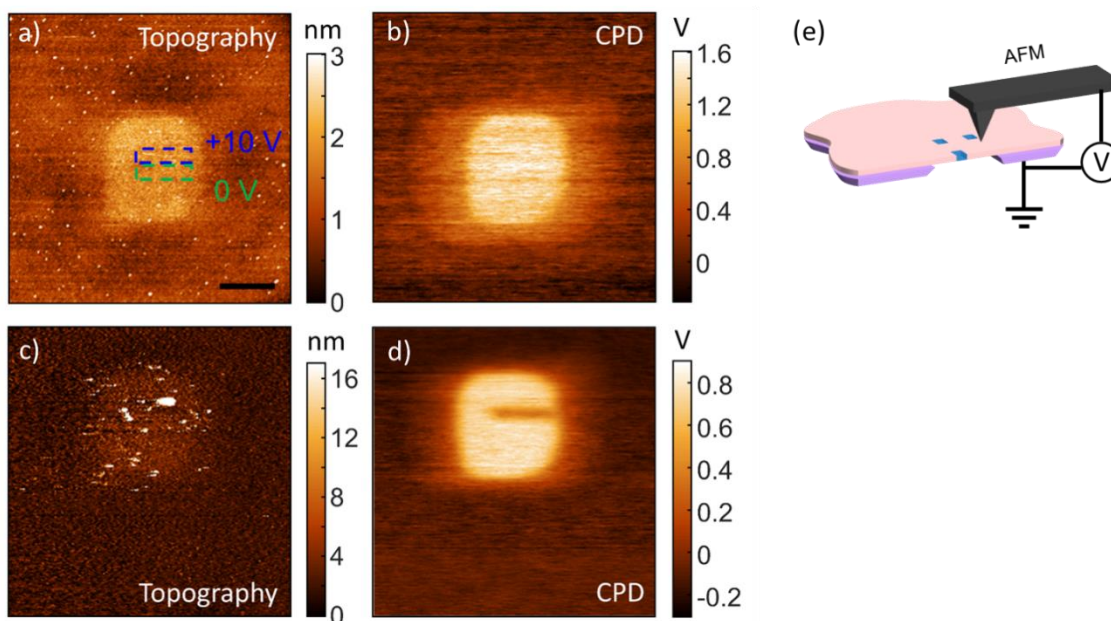


Figure S6. Reactivity of implanted lithium. (a)-(b) Topographic and KPFM images of a lithiated area on Si wafer ($1\mu\text{m} \times 1\mu\text{m}$, $F_{\text{Li}} \approx 100\text{ nm}^{-2}$). The two dashed $150\text{ nm} \times 500\text{ nm}$ boxes indicate regions that were scanned with a +10 V (blue) and 0 V (green) biased AFM tip in contact mode (while sample was grounded). (c)-(d) Topographic and CPD maps of the same area after biased scanning showing oxidation of the 10 V-scanned regions. The scale bars are 500 nm for all panels. The tip's quality has deteriorated due to the reactions run in contact mode, therefore the topographic image of panel (c) looks more noisy than in (a). Accumulation of surface particles is evident in (c), the expansion of the implanted region is otherwise unaffected outside the region scanned at 10 V on. (e) Schematic shows the electrical configuration of biased tip scanning.

VI. Thermal activation

In addition to the voltage bias or e-beam irradiation activation of implanted Li^+ described in the main text, thermal activation can also be used to induce local reactions and ion diffusion. Various transformations can be observed in lithiated annealed Si membranes depending on the Li dose and the imaged side of the membrane. At lower doses, the back (opposite-to-implantation) side of the membrane has a nicely-outlined expansion, corresponding to the implanted area (Fig. S7a) and a matching elevated CPD region (Fig. S7b) After annealing at 700 °C (*i.e.*, at a temperature higher than the melting point of the most refractory bulk lithium silicide phase) in argon, the implanted region and its surroundings develop outgrown nanocrystals, with minimal expansion (Fig. S7c-d). For higher doses, implantation leads to formation of a “blanket layer” area on the membrane side opposite to implantation – an elevated mesa of very high CPD (Fig. S7e-f). Formation of this layer must be related to spillage of the implanted ions onto the back side of the membrane (the surface opposite to the incident FIB). Upon annealing at 700 °C, this layer also develops nanocrystals, but also significantly expands laterally, indicating that the surface diffusion of Li^+ is facilitated relative to the bulk. On the front side of the membrane (facing the FIB), where mounds are grown (Fig. S7i-j), these melt upon heating, deform and expand laterally forming a jagged front (Fig. S7k-l).

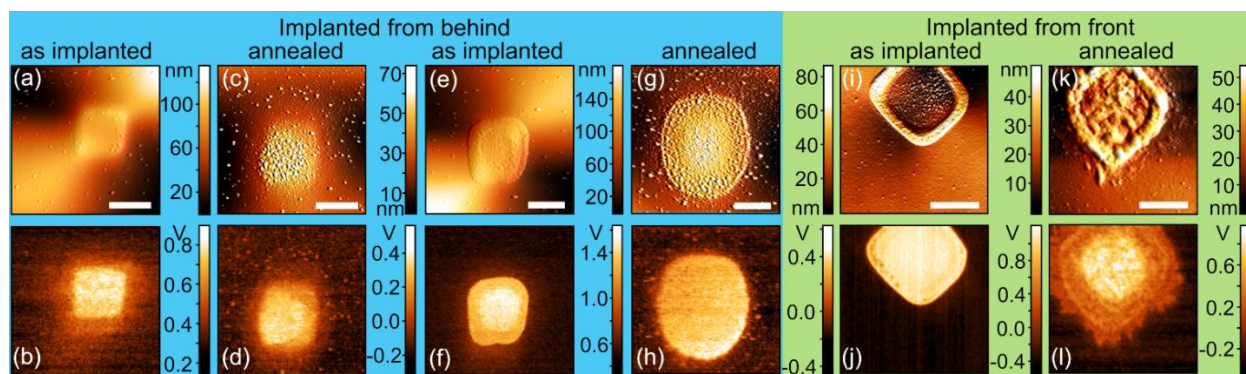


Figure S7. Thermal activation of the lithiated areas. KPFM topographic ((a)-(k), top row) and CPD ((b)-(l), bottom row) images of Si membranes lithiated from the back (blue background) and front (green background), and imaged from the front before and after annealing in an argon-filled glove box. All implanted areas were $1 \mu\text{m} \times 1 \mu\text{m}$. Area shown in (a)-(d) had a fluence of 3400 nm^{-2} and was annealed for 5 min. at 700 °C and 20 min. at 500 °C. Area shown in (e)-(h) had a fluence of 5000 nm^{-2} and was annealed for 5 min. at 700 °C and 20 min. at 500 °C. Area shown in (i)-(l) had a fluence of 950 nm^{-2} and was annealed for 75 min. at 150 °C. Clearly, annealing activated Li^+ diffusion, formation of nanocrystallites and reaction of the mounds with the underlying silicon.

If the dose is high ($> 500 \text{ nm}^{-2}$), and the sample did not have enough time to oxidize, the annealed mounds break into a pattern of interconnected nano-puddles of solidified liquid, which does not wet the surface well. Figure S8a-b shows AFM topographic images of such a case before

and after annealing (at 400 °C in argon), respectively. The same happens on a Ga⁺ FIB milled surface, shown in SEM images of Figure S8c-d. The bulk Si wafer surface was milled flat, but upon annealing, it got flooded with liquid, flowing from under the exposed lithiation mounds. Since these liquid-like patterns appear after annealing at a low temperature, well below the melting point of any known stable lithium silicide (Li₂₂Si₅, m.p. 628 °C), silicon itself (m.p. 1414 °C), platinum (m.p. 1768 °C), lithium oxide (m.p. 1438 °C, hydroxide (m.p. 462 °C), lithium silicate (m.p. 1024 °C), lithium carbonate (m.p. 723 °C). The only known material that could be present in the mounds and has a melting point below 400 °C is metallic lithium (m.p. 181 °C). This fact supports the proposed mound formation model, which assumes build-up of metallic lithium in the mounds.

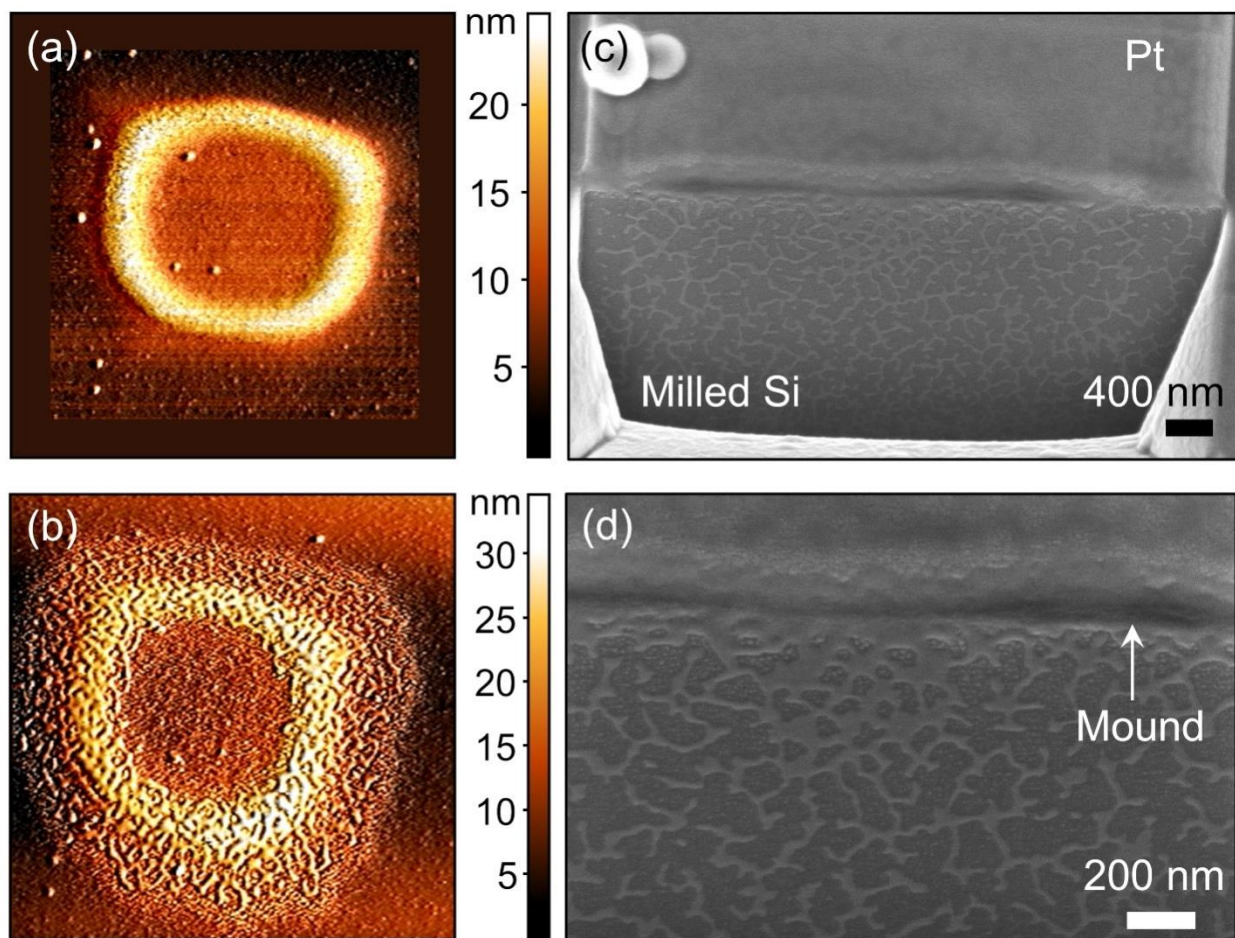


Figure S8. Evidence for metallic Li in the mounds. (a) and (b) topographic images of a 1 μm × 1 μm lithiated area on a bulk SOI wafer ($F \approx 550 \text{ nm}^{-2}$) before and after annealing (at 400 °C for 10 mins., in argon), respectively. Clearly, the mounds partly melted forming a pattern of interconnected nano-puddles poorly wetting the surface. (c) and (d) are SEM micrographs of a lithiated area (1 μm × 1 μm, $F \approx 1900 \text{ nm}^{-2}$) on bulk Si wafer capped with Pt, Ga⁺ FIB milled and

then annealed at 400 °C for 15 min. in an argon-filled glove box. The milled Si surface, which was smooth prior to milling, is covered with a network of nano-puddles clearly originating from the lithiated area above it.

VII. Mound-free implantation

The desirable outcome of Li^+ implantation is a uniform distribution of lithium inside the implanted material, without spillage onto the surface and formation of peripheral mounds. Our preliminary tests indicate that this goal can be achieved by cooling down the sample during implantation to suppress diffusion of ions to the surface. Figure S9a-b show KPFM images of a bulk Si area that was implanted while the sample was cooled down to -80 °C with a Peltier cooling stage. A clear uniform vertical expansion of the Si in the implanted area is seen, with a matching elevated CPD region, indicative of the absence of bulk-surface lithium segregation. Another route for uniform implantation is using other materials. For example, metallic gold (Fig. S9c-d) shows little topographic changes upon lithiation, and a rich CPD map, indicating Li^+ distribution.

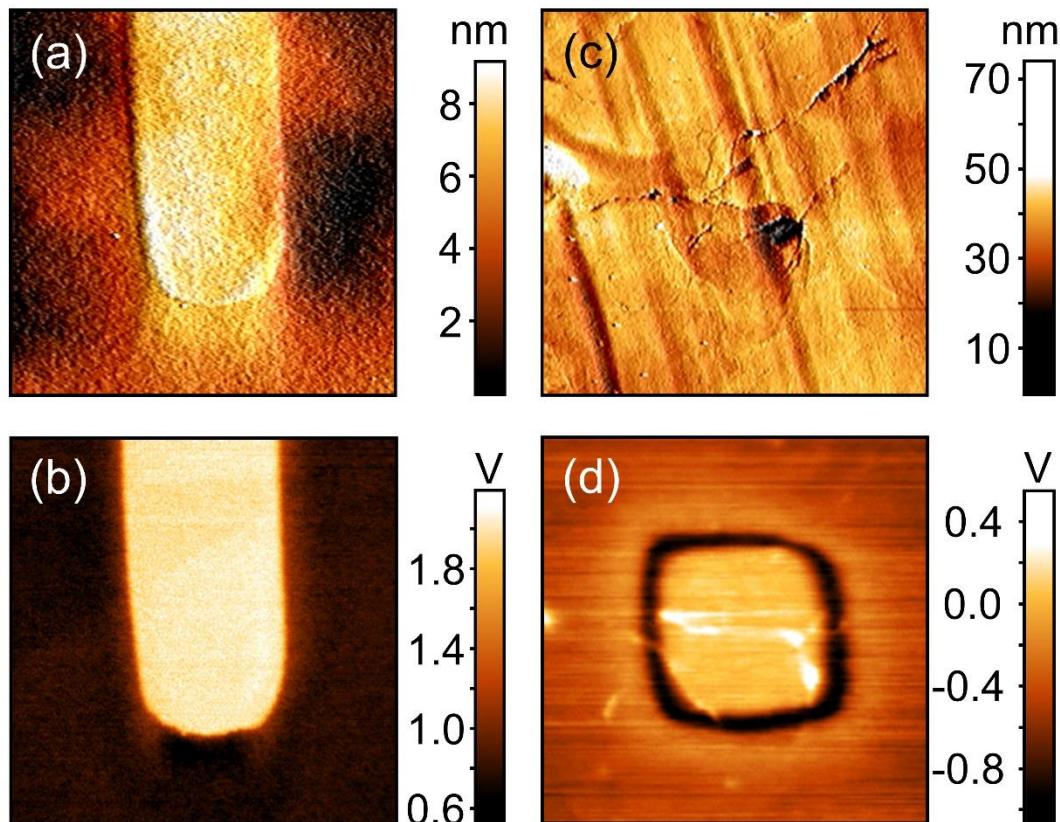


Figure S9. Mound-free implantation. (a)-(b) Topographic and CPD images of a part of the $1\ \mu\text{m} \times 10\ \mu\text{m}$ area, lithiated ($F \approx 560\ \text{nm}^{-2}$) at sample temperature of -80 °C. The sample is bulk SOI wafer.

(c)-(d) Topographic and CPD maps of a $1\ \mu\text{m} \times 1\ \mu\text{m}$ area on gold surface lithiated at room temperature ($F_{\text{Li}} \approx 530\ \text{nm}^{-2}$).

VIII. Selected-area electron diffraction imaging

A selective-area electron diffraction (SAED) pattern from the area *A* (see Figure 4 in main text) confirms high crystallinity of the diamond type *c*-Si matrix and reveals barely visible diffuse contours (white arrows) along [100] and [010] directions between the Bragg reflections assigned to ordering of clusters formed by interstitials, which occupy tetrahedral positions in the *c*-Si crystal lattice.² Because of structural disruption caused by implantation, no diffuse contours are observed in the area *B*, instead two diffuse rings (large blue arrows in Fig. S10) arise likely due to amorphized metastable Li_xSi . The rings correspond to the most probable interatomic spacings of 0.32 nm and 0.18 nm, which are consistent with a disrupted glass-like Li_xSi alloy coexisting with *c*-Si and supported by calculations for the tetragonal LiSi ($x=1$) phase performed for the Materials Project.³ For this phase, the calculated major (211) Bragg reflection corresponds to the lattice spacing of 0.337 nm and other two most intensive (312) and (501) diffraction peaks correspond to the spacings of 0.206 nm and 0.177 nm, respectively. The observed broad rings satisfactorily match to these two groups of the LiSi lattice spacings.

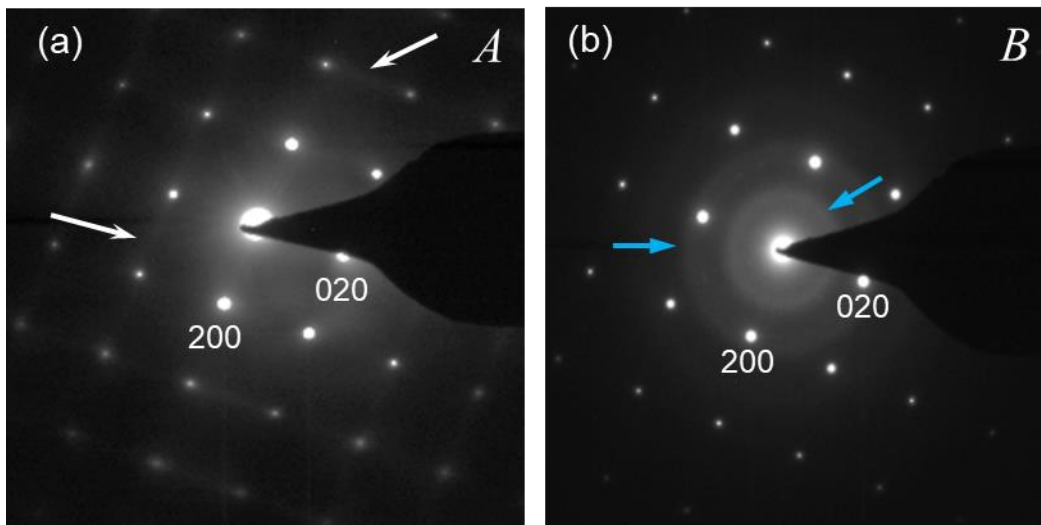


Figure S10. SAED patterns of silicon membrane after implantation. Pristine region *A* (a) and lithiated region *B* (b) as in Figure 4 from the main text; zone axis $B = [001]$.

REFERENCES

- (1) Wang, F.; Graetz, J.; Moreno, M. S.; Ma, C.; Wu, L.; Volkov, V.; Zhu, Y. Chemical Distribution and Bonding of Lithium in Intercalated Graphite: Identification with Optimized Electron Energy Loss Spectroscopy. *ACS Nano***2011**, *5*, 1190–1197.
- (2) De Ridder, R.; van Tendeloo, G.; Amelinckx, S. A Cluster Model for the Transition from the Short-Range Order to the Long-Range Order State in F.C.C. Based Binary Systems and Its Study by Means of Electron Diffraction. *Acta Crystallogr. A***1976**, *32*, 216–224.
- (3) Jain, A.; Ong, S. P.; Hautier, G.; Chen, W.; Richards, W. D.; Dacek, S.; Cholia, S.; Gunter, D.; Skinner, D.; Ceder, G.; Persson, K. A. Commentary: The Materials Project: A Materials Genome Approach to Accelerating Materials Innovation. *APL Mater.***2013**, *1*, 011002.